Fatigue & Fracture of
Engineering Materials & Structures

doi: 10.1111/j.1460-2695.2010.01492.x

Coherent gradient sensing (CGS) method for fracture mechanics: a review

H. V. TIPPUR

Department of Mechanical Engineering, Auburn University, AL 36849, USA

Received in final form 04 January 2010

ABSTRACT It has been 20 years since the introduction of coherent gradient sensing (CGS) technique for studying fracture problems. In this article, an up-to-date review of this full-field optical method as an experimental fracture mechanics tool is presented. The primary focus here is on contributions of the method to the advancement of fracture mechanics in general and dynamic fracture behaviour of materials in particular. Optical results published by various investigators using CGS to understand fracture of homogeneous materials, bimaterials, particulate composites, fibre reinforced composites and functionally graded materials are reviewed. A few promising new developments such as applications to load bearing problems and combining CGS with other full-field optical methods to enhance its measurement capabilities are also visited.

Keywords composite materials, contact stresses, experimental fracture mechanics, functionally graded materials, optical metrology, particulate composites.

INTRODUCTION

Historically, the full-field optical methods such as photoelasticity, optical caustics and moiré interferometry have played a crucial role in the progress of fracture mechanics in general and dynamic fracture mechanics in particular. The method of coherent gradient sensing (CGS) has been a new addition to the cadre of full-field optical techniques used in experimental fracture mechanics investigations in the past two decades. This method was developed and demonstrated in 1989 by the author and his colleagues[1] to measure surface slopes or in-plane stress gradients in planar solids. The mechanical fields measured by this method being identical to the ones that produce optical caustic curves (or, the shadow-spot) caused by stress concentrations in planar solids, the potential of the method to study fracture mechanics problems was obvious right from its conception. However, unlike the method of caustics, CGS offered full-field measurement capability with the help of a relatively simple optical arrangement to quantify crack tip deformations. Soon its potential for dynamic fracture investigations became evident when it was demonstrated successfully by employing a pulsed laser (instead of a CW laser) as a coherent strobe light source and a high-speed camera as a recording devise. Subsequently, CGS was employed to study dynamic fracture in optically isotropic transparent plastics and opaque metallic sheets. An optical study of dynamic crack growth along dissimilar material interfaces under stress wave loading conditions led a period of widespread use of the method to study subsonic and intersonic crack growth in bimaterials. Investigation of impact induced fracture of fibre reinforced composites, static and dynamic fracture of functionally graded particulate composites and structural foams, and dynamic crack-inclusion interactions, all using CGS as a measurement tool, have also ensued in the intervening years. CGS has also been employed by a few investigators in conjunction with other optical techniques such as photoelasticity and moiré interferometry to augment its capabilities for future fracture mechanics investigations.

In this article, the description of the method and its applications to various fracture mechanics applications over the years is reviewed. After describing a typical optical set-up for implementing CGS, the governing equations for the method are presented in a planar setting. Aspects of optical alignment to execute the method successfully are discussed further. An overview of contributions of different investigators to fracture mechanics using CGS

Correspondence: H. V. Tippur. E-mail: htippur@eng.auburn.edu

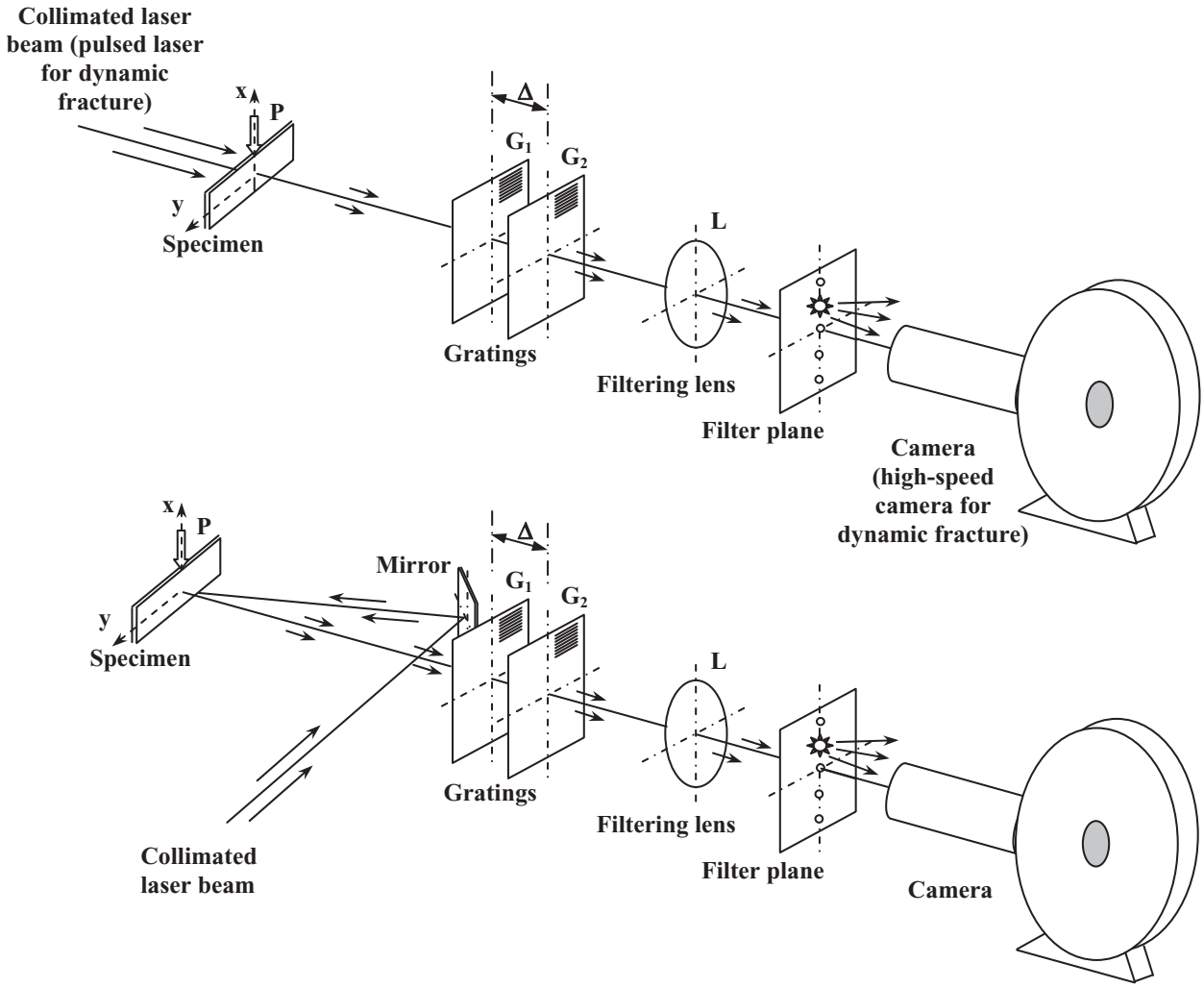

Fig. 1 Optical arrangement for implementing CGS in dynamic fracture mechanics studies using transmission and reflection CGS. (For quasi-static studies a CW laser light and a SLR camera back can be used in place of pulsed laser light and high-speed camera.)

is presented in the final sections before summarizing the accomplishments to date.

OPTICAL SET-UP AND IMPLEMENTATION DETAILS

Two representative experimental set-ups for fracture investigation of planar optically transparent and opaque objects using CGS are shown schematically in Fig. 1. They consist of a collimated coherent light beam, a pair of Ronchi gratings, a filtering aperture, a positive lens and a camera back. In case of an opaque solid, the object surface needs to be flat and mirror-like. A collimated laser beam of diameter larger than the region of interest is used to illuminate the object. For dynamic fracture studies, a pulsed laser beam is used as a coherent strobe light illumination.* The object waves transmitted through or reflected off the object surface propagate through two parallel Ronchi gratings (G_1 and G_2) that are spatially separated (separation distance denoted by Δ) along the optical axis. The resulting diffracted wave fronts are collected by a positive lens (L) and the diffraction (Fourier) spectrum is registered on its back focal plane (or the filter plane) as shown. An aperture is used to filter out all but the necessary diffraction orders of the spectrum. The resulting interferograms are recorded in real-time using a conventional or a high-speed camera depending up on whether quasi-static or a dynamic fracture study is being carried out. It should be emphasized that the camera

* Most reports to date have used an Argon-ion pulse laser with an acousto-optic shuttering device to produce short duration (25–50 nsec) repeating light pulses (1–10 μsec intervals).

system comprising of the positive lens and the image plane of the camera needs to be focused on the object surface during the initial optical alignment. That is, the object and the image distances in the set-up obey the lens law.

The gratings used for CGS are typically chrome-on-glass depositions with a rectangular transmission profile, or the so-called Ronchi gratings. (The choice of Ronchi gratings is based on commercial availability or ease of fabrication using microlithography but other grating profiles could be used as well. Typical grating densities used are in the range of 20–40 lpmm (or, 500–1000 lines pairs per inch)). Anti-reflection coatings on Ronchi gratings (on the chrome deposited faces) are essential for minimizing optical noise due to multiple reflections in the gap between the two gratings. Other parameters, such as grating pitch, grating separation distance and focal length of the imaging lens are chosen based on the need for (i) producing sufficient spatial shearing of the object wave front without compromising the accuracy of derivative representation of the measured mechanical fields and (ii) spatially resolving the diffraction spots on the back focal plane of the imaging lens for filtering the optical signal. (The use of micro-positioning devices to achieve in-plane and out-of-plane parallelism between the two gratings limit the smallest grating separating distance to about 15 mm in most reported studied to date.)

The surface preparation of opaque planar objects for reflection-mode CGS study also needs special attention. The surface of the test sample should be made optically flat and specularly reflective in the region of interest. If the specimen is made of a metallic material, lapping the surface flat followed by an aluminium or gold film deposition for achieving good reflectivity is recommended. On the other hand, if the material being studied is a polymer or a composite that cannot be readily lapped and polished, an alternative method could be adopted. The specimen surface is first machined flat and tool marks are removed (say, by sanding the surface using successively finer grade sandpapers). Subsequently, an optical flat (commercially available borosilicate glass disk), previously deposited with a thin layer of aluminium or gold (using a thermal evaporator or a sputtering device) film, is used to transfer the metal film deposition to the specimen surface. The transferring of metal film can be done using a suitable adhesive such as low-viscosity epoxy that bonds relatively strongly with the aluminium film when compared to the optical flat. This process is depicted in a self-explanatory schematic in Fig. 2. The thickness of the adhesive should be minimum, a few micrometers, to avoid potential shear-lag effects.

The CGS interferometer needs to be precisely aligned to ensure (i) the planarity of the incident laser beam used for interrogating the object and (ii) the parallelism of the Ronchi gratings (G_1 and G_2 in Fig. 1) as well as the grating

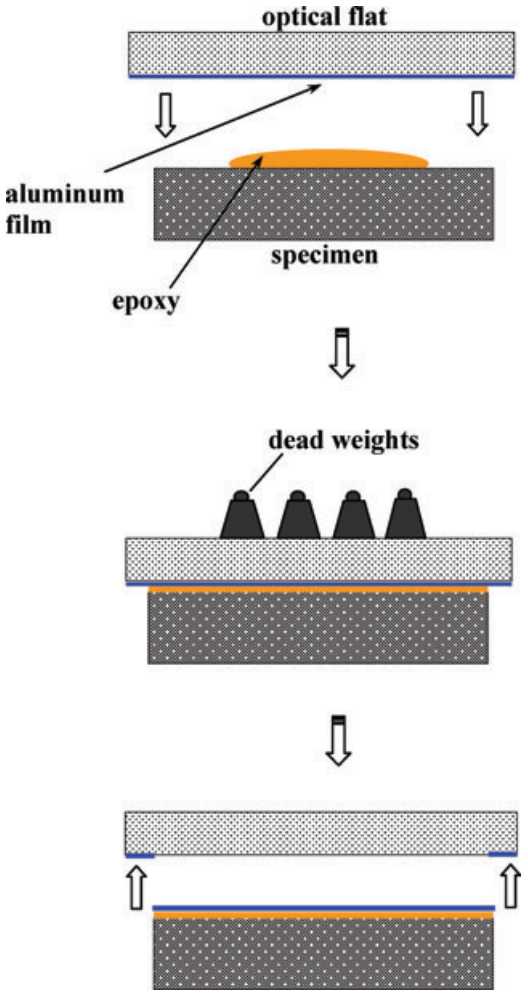

Fig. 2 Schematic depicting aluminizing an opaque specimen surface to obtain a mirrored surface for reflection CGS study.

lines. This is accomplished by mounting gratings G_1 and G_2 on micro-positioning devices. Typically, one of the two gratings, say G_2, is mounted on a device with translational capability in the z-direction and rotational capability about the z-axis. Separate coarse rotational capabilities about the x- and the y-axes for G_1 are also preferable. First, parallelism between gratings G_1 and G_2 can be ensured using the coarse positioning device for G_1 by rotating it relative to G_2 about the x- and the y-axes. A high-degree of initial collimation of the laser beam can then be ensured using a front-coated mirror with a good flatness, (say, a $\lambda/8$-mirror) as the reference surface during optical alignment. Assuming good parallelism between grating lines of G_1 and G_2, when the incident beam is not a collimated beam and is a spherical wave front, $i(x, y) = x^2 + y^2/2f$, f being the focal length of the collimating lens, a fringe pattern similar to the one shown in Fig. 3a appears on the image plane when the principal direction of the Ronchi

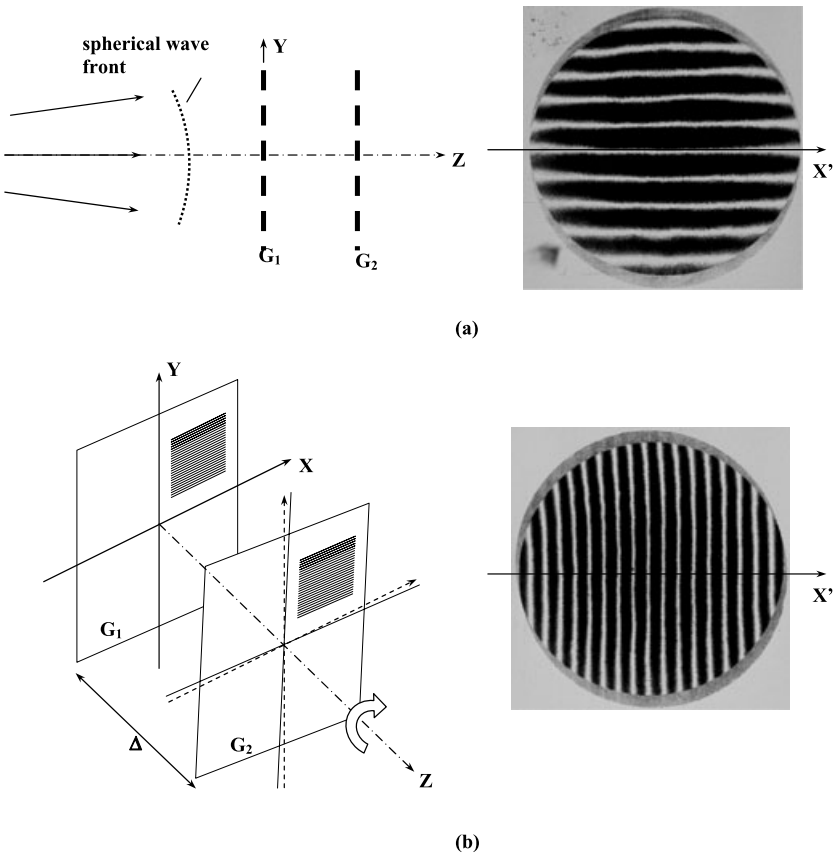

Fig. 3 Typical alignment fringes seen when the principal direction of the gratings is along the *y*-axis. (a) Fringes due to non-collimated (or spherical) wave front and, (b) fringes due to rotational misalignment between gratings G_1 and G_2.[4]

gratings is along the *y*-axis. Now, a planar wave front can be obtained by translating the collimating lens relative to the point source (pin-hole) until the fringe spacing increases gradually covering the entire field-of-view as a uniform bright field/fringe. For a planar wave front incident on the gratings, the rotational misalignment (about the optical axis) between the two gratings would result in equally spaced fringes approximately along the principal direction of the gratings, as the one shown in Fig. 3b. These fringes can be eliminated by rotating, say, G_2 about the *z*-axis until the fringe spacing increases and a single bright fringe occupies the entire field-of-view. In practice, however, both these misalignments typically co-exist resulting in equally spaced fringes oriented at an arbitrary angle relative to the principal direction of the two gratings. Hence alignment will have to be carried out iteratively until a uniform bright fringe covers the entire field-of-view.

GOVERNING EQUATIONS

A detailed derivation of the governing equations for the CGS interferometer based on a first-order diffraction analysis was provided by Tippur *et al.*[1,2] Subsequently a higher order Fourier optics analysis was presented by the author.[3] In the following, a simpler geometric analysis based on diffraction theory[4] is presented for completeness.

Upon reflection from the object surface or transmission through the thickness of the planar object, the object wave front is incident on the grating G_1 as shown in Fig. 4. The information regarding deformation of the planar object is encoded in the form of local non-planarity of the initially collimated incident beam. Let the perturbed object wave making an angle ϕ with the optical axis in the *y*–*z* plane be transmitted through gratings G_1 and G_2 of pitch *p* with principal grating direction, say, along the *y*-axis. The separation distance between the two gratings along the optical axis (the *z*-axis) be Δ. The diffracted light beam emerging from the first grating consists of a zero and several odd diffraction orders, each denoted by the corresponding complex amplitude distribution *E*. For simplicity of analysis consider three diffraction orders E_0, E_{+1} and E_{-1} after the first grating G_1. These waves propagate in discretely different directions according to the diffraction equation $\theta = \sin^{-1}(\lambda/p) \approx (\lambda/p)$ for small angles. Each of these diffracted wave fronts diffract once again as they pass through the second grating G_2 and the corresponding nine wave fronts propagating in several discrete directions are denoted by $E_{(i,j)}$ ($i = 0, \pm 1$, $j = 0, \pm 1$) where the first subscript corresponds

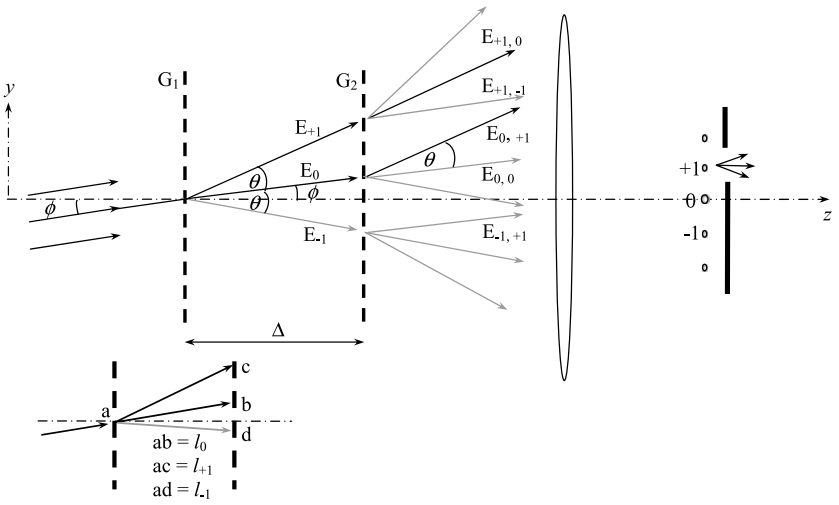

Fig. 4 Schematic representation of diffraction of light waves and Fourier filtering of light waves in a CGS set up.

to diffraction order at the first grating G_1 and the second subscript at the second grating G_2, respectively. The wave fronts $E_{(\pm1,0)}$ and $E_{(0,\pm1)}$ contribute to ±1 diffraction spot on the focal plane. (And, the diffracted wave fronts $E_{0,0}$, $E_{+1,-1}$ and $E_{-1,+1}$ contribute to the zeroth order.) By letting ±1 diffraction order to pass through the filtering aperture (+1 order is being let through the filter in Fig. 4), interference fringes resulting from the corresponding complex amplitudes can be evaluated. To do this, let l_0 and $l_{\pm1}$ denote the optical path lengths of E_0 and $E_{\pm1}$, respectively, between the two gratings. Then, the complex amplitudes E_0 and $E_{\pm1}$ can be represented as $E_0 = A_0 \exp(ikl_0)$, $E_{\pm1} = A_{\pm1} \exp(ikl_{\pm1})$ where A's denote amplitudes, k is the wave number ($=2\pi/\lambda$) and $i = \sqrt{-1}$. Noting that no additional path difference between these two waves occurs beyond G_2, the intensity distribution on the image plane for a 1:1 magnification is proportional to

$$\begin{aligned} I_{\pm1} &= (E_{0,\pm1} + E_{\pm1,0})(E_{0,\pm1} + E_{\pm1,0})^* \\ &= A_0^2 + A_{\pm1}^2 + 2A_0A_{\pm1}\cos k(l_0 - l_{\pm1}), \end{aligned} \tag{1}$$

when ±1 diffraction spot is let through the aperture at the spectrum plane. In the aforementioned, $(\bullet)*$ denotes the complex conjugate. From the geometry, the optical path lengths l_0 and $l_{\pm1}$ can be expressed as

$$\begin{aligned} l_0 &= \frac{\Delta}{\cos\phi} = \frac{\Delta}{\left(1 - \frac{\phi^2}{2!} + \frac{\phi^4}{4!} - \cdots\right)}, \\ l_{\pm1} &= \frac{\Delta}{\cos(\theta \pm \phi)} = \frac{\Delta}{\left(1 - \frac{(\theta \pm \phi)^2}{2!} + \frac{(\theta \pm \phi)^4}{4!} - \cdots\right)}, \end{aligned} \tag{2}$$

by expanding $\cos(\bullet)$ in the neighbourhood of $(\bullet) =$ zero. For *small angles*, by neglecting the terms of the order of $(\bullet)^3$ and beyond, Eq. (2) can be written as

$$\begin{aligned} l_0 &\approx \frac{\Delta}{\left(1 - \frac{\phi^2}{2!}\right)} \approx \Delta\left(1 + \frac{\phi^2}{2}\right), \\ l_{\pm1} &\approx \frac{\Delta}{\left(1 - \frac{(\theta \pm \phi)^2}{2!}\right)} \approx \Delta\left(1 + \frac{(\theta \pm \phi)^2}{2}\right), \end{aligned} \tag{3}$$

using the binominal expansion.

Substituting for the path difference $(l_0 - l_{\pm1})$ from Eq. (3), the intensity distribution (Eq. (1)) on the

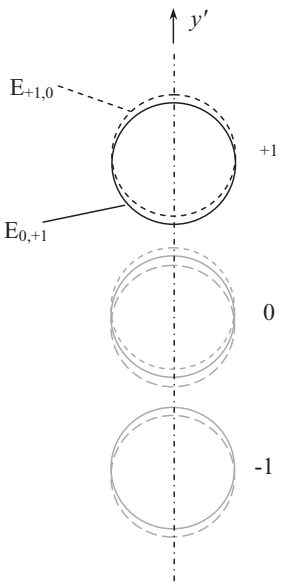

Fig. 5 Overlapping but sheared wave fronts on the image plane (x'–y' plane) for filtering all but +1, 0, −1 diffraction spots. The solid and broken circles correspond to zero order and +1 or −1 diffraction orders passing though the aperture, respectively. Each circle represented a circular beam of light.

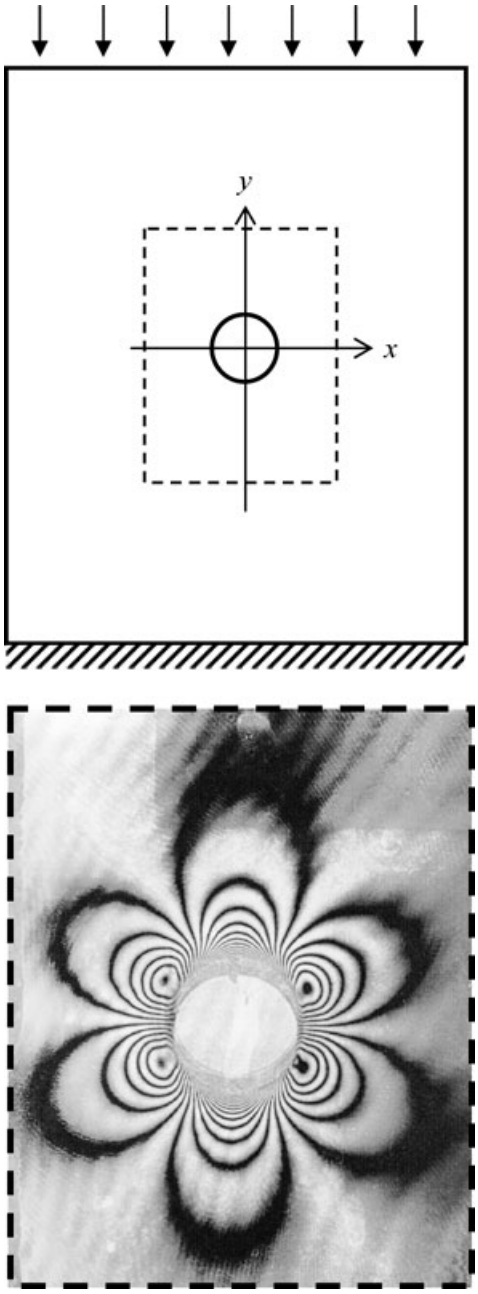

Fig. 6 Transmission CGS fringes representing contours of $\partial(\sigma_x + \sigma_y)/\partial y$ in the vicinity of a circular cut-out (diameter 12.5 mm) in sheet subjected to uniaxial loading. The trace of the periphery of the hole and its shifted counterpart in the y-direction can be readily seen.

image plane when ±1st diffraction order is allowed to pass through the filtering aperture becomes

$$I_{\pm 1} \approx A_0^2 + A_{\pm 1}^2 + 2A_0A_{\pm 1}\cos\left[k\Delta\left(\frac{\theta^2}{2} \pm \theta\phi\right)\right]. \quad (4)$$

The constructive interference occurs when the argument of the cosine term in Eq. (4) is $2N_d\pi$ where $N_d = 0, \pm 1, \pm 2, \ldots,$ is the fringe order. Here the subscript d is used to emphasize that the fringe order corresponds to the deformed object wave front. By substituting for the wave number and simplifying a relationship between experimental parameters and the angle ϕ can be obtained as

$$\frac{\Delta}{\lambda}\theta\left(\frac{\theta}{2} \pm \phi\right) = N_d. \quad (5)$$

When the specimen is in the unformed state ($\phi = 0$ in Eq. (5)), the fringe order of the initial uniform bright fringe can be denoted by $N_u = (\Delta/\lambda)\theta(\theta/2) = (\Delta/p)(\theta/2) =$ constant ($N_u = 0, \pm 1, \pm 2, \ldots,$), using $\theta \approx \lambda/p$. By incorporating the expression for N_u in Eq. (5), the magnitude of angular deflection of light beam locally on the surface can be written as

$$\phi = (N_d - N_u)\frac{p}{\Delta} = N\frac{p}{\Delta},$$

or,

$$N = (N_d - N_u) = 0, \pm 1, \pm 2, \ldots \quad (6)$$

In the aforementioned, it is not necessary that the value of N_u (the initial fringe order) is known as long it is a constant over the entire field of view. Thus, N in Eq. (6) represents fringe orders relative to the initially planar surface.

The fringe formation in the overlapping region can be schematically represented as shown in Fig. 5 where solid line is used to represent the un-diffracted wave after G_2 and the dotted line represents either +1 or –1 order wave front. From Eq. (6) it is clear that the sensitivity of the interferometer for measuring angular deflections of light rays depends on the ratio of the grating pitch p and the grating separation distance Δ. This in turn offers a degree of experimental flexibility for altering measurement sensitivity by appropriately choosing experimental parameters p and/or Δ, an added advantage over other full-field methods used in fracture mechanics. (More often than not, it is convenient to vary Δ instead of p.) Also, it should be noted that interference fringes obtained by filtering all but +1 or –1 diffraction orders can be interpreted as forward and backward differences of the optical signal.

The angular deflections of light rays can be related to surface deformations of the object. Let the propagation vector of the object wave front be $\underline{d} = \frac{\partial(\delta S)}{\partial x}\underline{e}_x + \frac{\partial(\delta S)}{\partial y}\underline{e}_y + \underline{e}_z$ where δS denotes optical path difference and $\underline{e}_i$ is a unit normal in the ith direction. When light rays are described in the y–z plane, $\frac{\partial(\delta S)}{\partial y} \approx \phi$ for small angles.

When a transparent object is inspected using transmission CGS, the optical path S through the specimen is $S = (n-1)B$ where n is the refractive index of

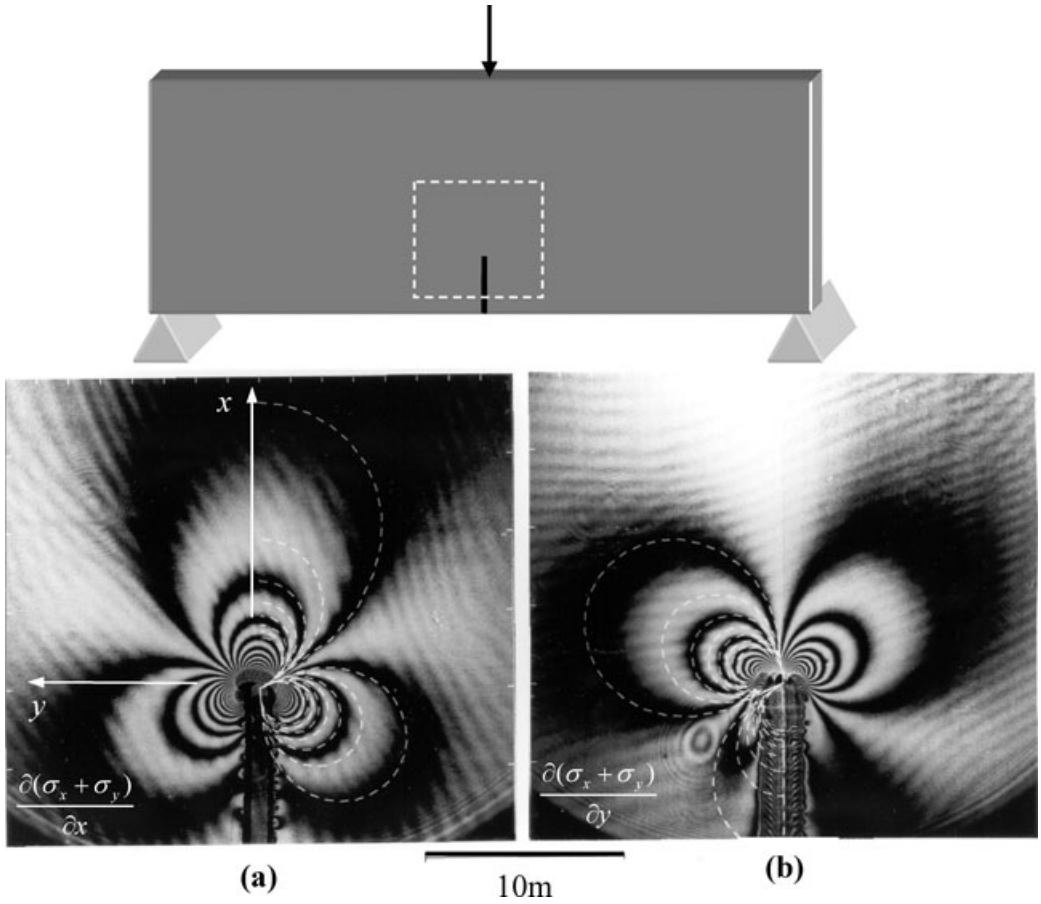

Fig. 7 Transmission CGS fringes representing stress gradients near a notch tip in a three-point symmetric bend PMMA specimen. The superposed dotted lines on the fringes correspond to synthetic CGS contours based on least-squares analysis of fringe data outside the crack tip 3D zone using Williams' asymptotic expansion for crack tip stresses.

the material and B is the thickness of the planar object in the unstressed state. Upon deformation, the optical path length becomes $S + \delta S$ where $\delta S = C_\sigma B(\sigma_x + \sigma_y)$, $C_\sigma = (-\frac{\nu}{E} + C_o)(n-1)$ is the elasto-optic coefficient and C_o is a stress-optic constant of the material. It should be noted that C_σ accounts for stress induced refractive index changes as well as thickness changes due to the Poisson effect. Thus, angular deflections of light rays in transmission CGS relate to the mechanical fields as

$$\phi \approx \frac{\partial(\delta S)}{\partial y} = C_\sigma B \frac{\partial(\sigma_x + \sigma_y)}{\partial y} = N\frac{p}{\Delta}, \qquad N = 0, \pm 1, \pm 2, \ldots \tag{7}$$

Thus, in transmission CGS, fringes are proportional to the gradient of the trace of the stress tensor of a planar solid in the direction of wave front shearing. An example of fringes around a circular stress concentration in a large PMMA sheet subjected to uniaxial compression in the far-field is shown in Fig. 6. Highly discernible and symmetric fringes surround the periphery of the stress concentration and the far-field is occupied by an easily recognizable bright zero order fringe. The rest of the fringes can be ordered using the boundary conditions of the problem.

When an optically opaque object is studied using reflection CGS, the optical path difference is $\delta S = 2w$, where w is the out-of-plane displacement along the z-direction. Then, angular deflections can be related to the mechanical fields as

$$\phi \approx \frac{\partial(\delta S)}{\partial y} = 2\left(\frac{\partial w}{\partial y}\right) = N\frac{p}{\Delta}, \quad N = 0, \pm 1, \pm 2, \ldots, \tag{8}$$

where w is the out-of-plane deflection of the wafer in the z-direction. Thus, in reflection CGS surface slopes in the direction of wave front shearing are obtained as fringes.

CGS AS AN EXPERIMENTAL FRACTURE MECHANICS TOOL

In the following, an overview of experimental fracture mechanics studies carried out using CGS by various investigators since its inception is presented. The

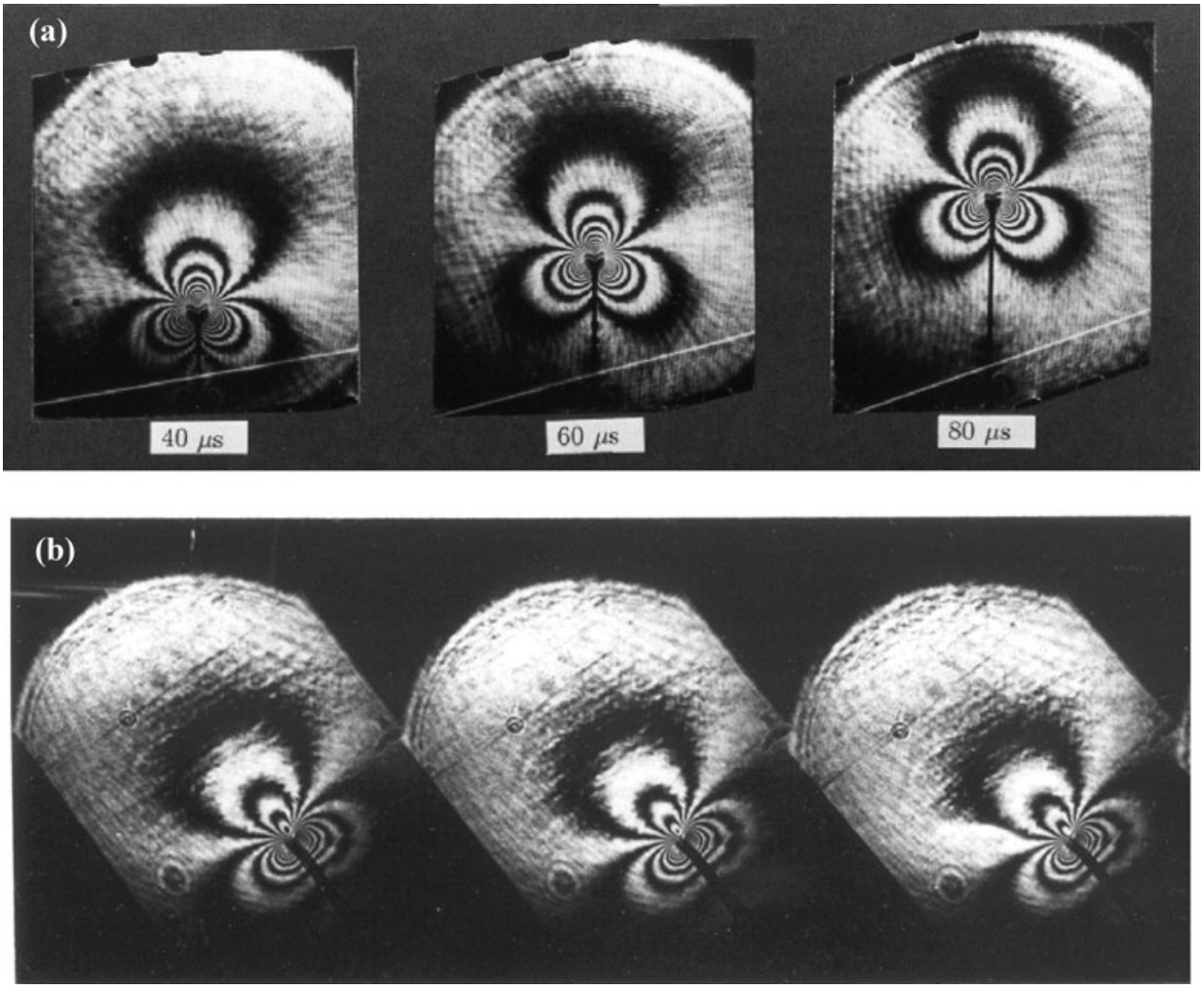

Fig. 8 Selected transmission CGS (a) and reflection CGS (b) interferograms at different instants of dynamic growth in a PMMA sheet impact loaded in a drop-tower (impact velocity 2m/sec) in 3-point bend configuration. Recorded at 100,000 frames per second and exposure time 25 nsec. Fringes are proportional to $\partial(\sigma_x + \sigma_y)/\partial x$ in (a) and $\partial w/\partial x$ in (b) where x is along the crack direction.[2,6]

description is categorized based on material types namely homogeneous materials, bimaterials, fibre reinforced composites, particulate composites, functionally graded composites undergoing quasi-static or dynamic loading. A few applications of CGS to study load bearing problems are also included. Efforts of various investigators to combine CGS with other optical methods to extract more information than the one from CGS alone are reviewed at the end.

Fracture of homogeneous materials

The first demonstration of CGS to study fracture mechanics was made in the reflection mode by Tippur *et al*.[1] In their work, crack tip surface slopes in the direction of an edge crack in a lapped and polished AISI 4340 steel sheet subjected to static three-point symmetric bending were measured for different statically applied loads. A good agreement between mode-I stress intensity factors evaluated from surface slope fringes ($\partial w/\partial x$, $\partial w/\partial y$, x-being the crack direction) at discrete fringe locations outside the zone of dominant crack tip triaxiality and the analytical results demonstrated the feasibility of CGS to experimental fracture mechanics investigations. In a follow-up publication,[2] the same authors proposed transmission CGS to examine crack tip fields in transparent solids. An edge cracked Plexiglas sheet (284 mm × 126 mm × 9 mm sheet and different edge notch lengths) subjected to symmetric three-point bending was studied. The measured mode-I fringes proportional to crack tip stress gradients ($\partial(\sigma_x + \sigma_y)/\partial x$, $\partial(\sigma_x + \sigma_y)/\partial y$) (see Fig. 7) were analysed successfully to quantify stress intensity factors using

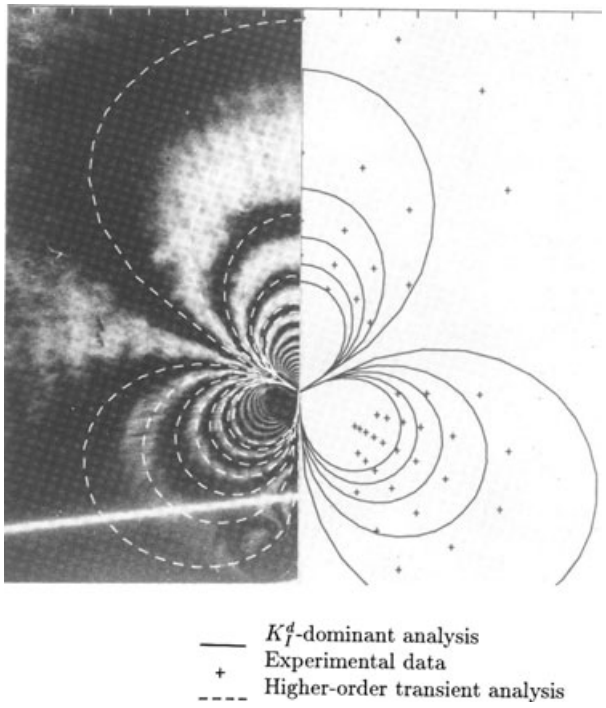

Fig. 9 Synthetic fringe patterns reconstructed from K-dominant (one-term) (solid lines) and higher-order (broken lines) transient analysis superposed on the corresponding transmission-mode CGS interferogram from a dynamic crack growth experiment on PMMA.[6]

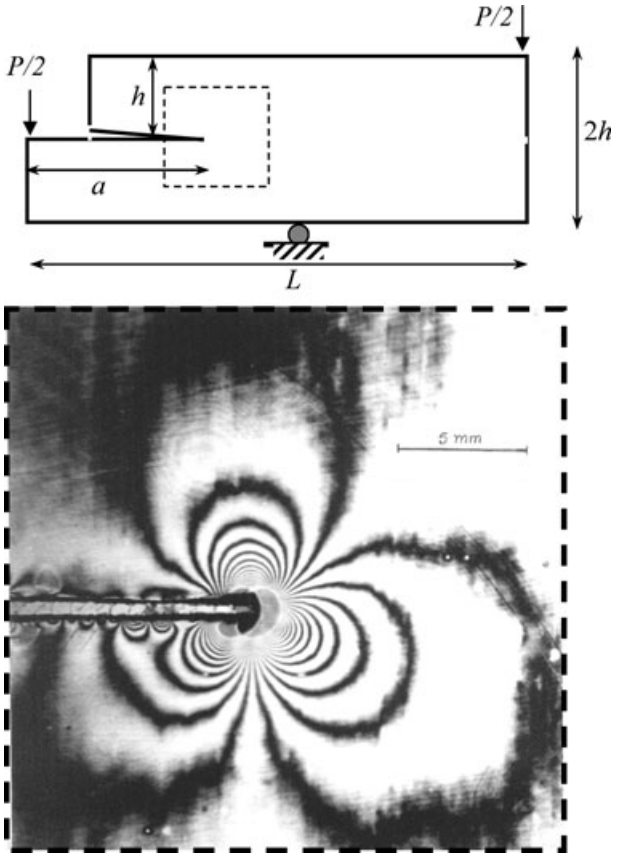

Fig. 10 Transmission CGS interferogram for a mixed-mode crack tip deformation in a modified flexural geometry.[3]

appropriate Williams' asymptotic expansions,

$$C_\sigma B\left(\frac{\partial(\sigma_x+\sigma_y)}{\partial x \text{ or } \partial y}\right) = C_\sigma B \sum_{N=1}^{\infty} A_N \left(\frac{N}{2}-1\right) \times r^{\left(\frac{N}{2}-2\right)} \begin{matrix}\cos \\ \sin\end{matrix} \left(\frac{N}{2}-2\right)\theta = M\frac{P}{\Delta}, \quad M = 0, \pm 1, \pm 2, \ldots, \tag{9}$$

where (r, θ) denote polar coordinates centred at the crack tip and A_N are the constant coefficients of the expansion with $A_1(k_I/\sqrt{2\pi})$ proportional to mode-I stress intensity factor K_I. This paper also presented three major breakthroughs that solidified CGS as a valuable photomechanics tool for fracture mechanics. First, the need for employing higher order terms in the Williams' crack tip asymptotic expansion field in the optical field analysis using CGS was revealed. For the first time, using CGS field quantities, identical to those which give rise to an optical caustic for a mode-I crack, the authors were able to demonstrate the deficiencies of shadow spot measurements based on only the singular stress terms of the asymptotic field.[2,5] Second, this work established a framework for performing linear overdeterministic least-squares analysis of CGS fringe data, routinely used until then by photoelasticians, to accurately extract fracture parameters by considering non-singular terms of an asymptotic expansion field. (The synthetic fringes generated using this approach and superposed as dotted lines on fringes in Fig. 7 demonstrate a close agreement between the two.) Third and possibly the most important, the feasibility of CGS to dynamic fracture mechanics investigations was demonstrated by coupling transmission CGS apparatus with a rotating mirror high-speed camera and a Argon-ion pulse laser to capture interferograms representing instantaneous stress gradients $(\partial(\sigma_x+\sigma_y)/\partial x)$ near a dynamically growing crack (~250 m/sec) in a PMMA sheet subjected to symmetric low-velocity impact (2 m/sec) loading in a drop-tower. Figure 8a shows a selection of interferograms recorded at 100,000 frames per second with an exposure time of 50 nsec from that experiment. Highly discernable fringes in these early experiments strongly hinted at the potential of the method for dynamic fracture investigations. An example of the same is shown in Fig. 9 where fringes from the CGS technique are superposed with the synthetic contours (superposed dotted lines) generated using overdeterministic analysis of optical data (discrete data points shown in the right-half) using a six-term

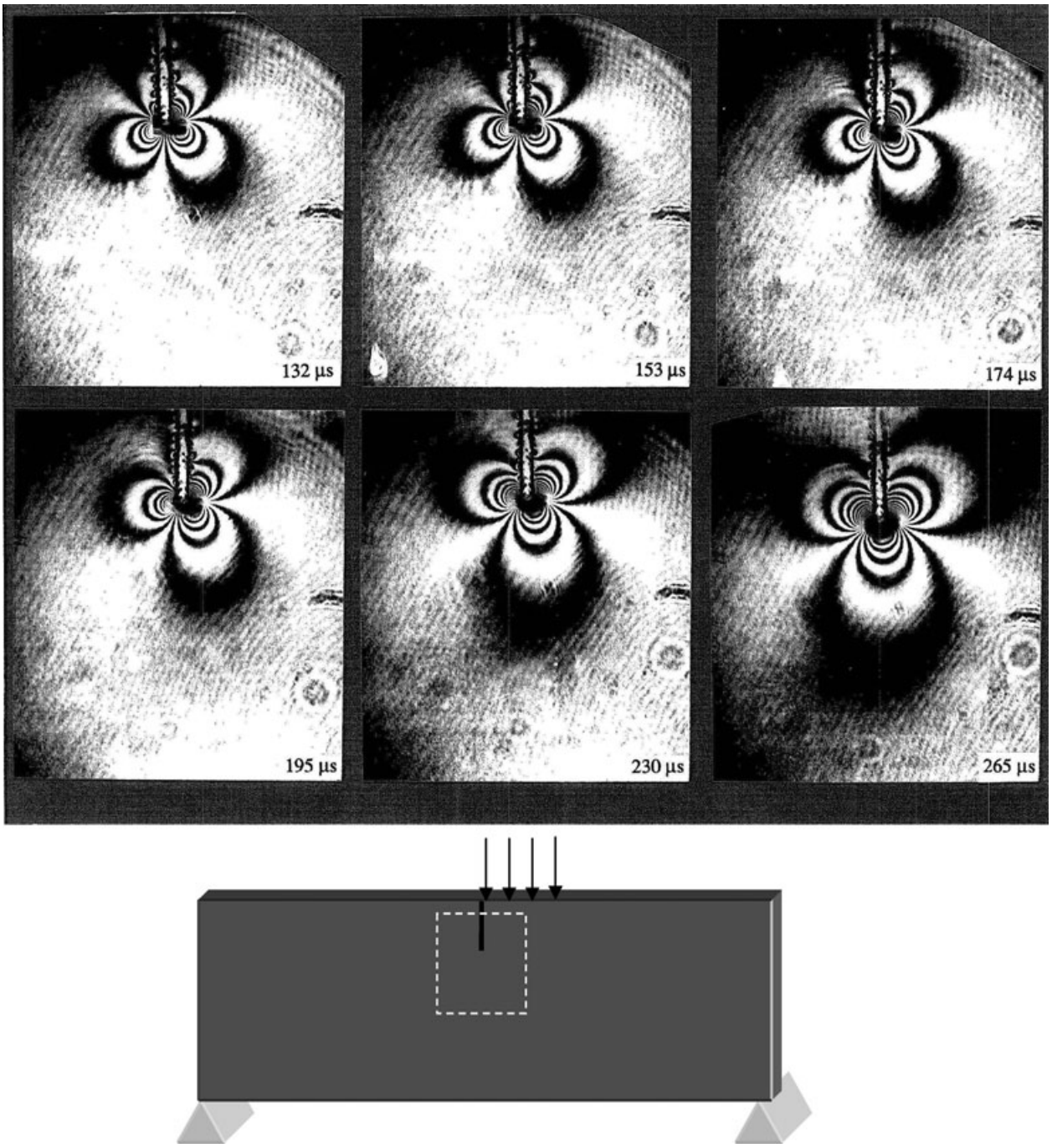

Fig. 11 Transmission CGS interferograms representing $\partial(\sigma_x + \sigma_y)/\partial x$ contours in a dynamic eccentric impact (see inset) experiment on a PMMA sheet with a edge notch subjected to mixed-mode loading. At early stages of impact, the crack is in dominant mode-II condition and transitions (as seen by the rotation of fringe lobes) to a dominant mode-I conditions with passage of time after initial impact. (Ref. [11], Courtesy A. J. Rosakis.)

asymptotic expansion for $(\sigma_x + \sigma_y)$ of a steadily growing crack. Also notable in this figure is that the optical data and synthetic contours are poorly correlated if K-dominance based on only the leading term of the asymptotic expansion is assumed.

Shortly after these initial successes with transmission CGS to study dynamic crack growth, the method was extended to the case of opaque solids using reflection CGS.[6] The effectiveness of the method in the reflection-mode was demonstrated by capturing surface slope $(\partial w/\partial x)$

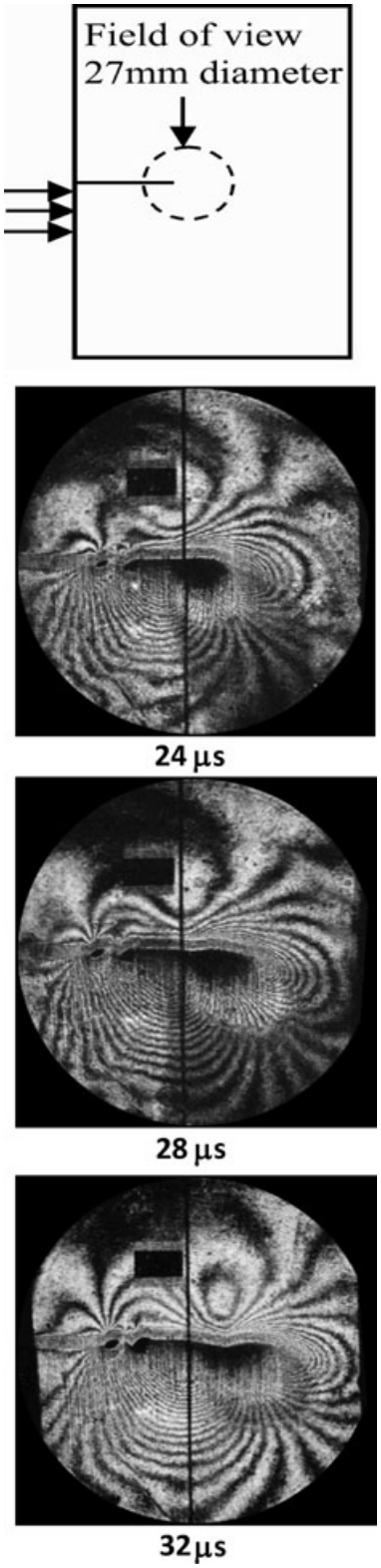

Fig. 12 A sequence of CGS interferograms in the vicinity of a propagating shear band from a pre-crack in C300 maraging steel subjected to impact loading as shown in the schematic. (Ref. [14], Courtesy: A. J. Rosakis.)

fringes around a dynamically propagating mode-I crack in a AISI-4340 steel and Plexiglas sheets subjected to symmetric low velocity impact loading in three-point bend configuration. In case of the former, the sample surface had to be lapped and polished to obtain a flat mirror-like surface finish whereas the surface of as-received stock was deposited with aluminium film in the latter. A few selected reflection CGS fringes from a PMMA sheet are shown in Fig. 8b. The optical results of these experiments were interpreted using conventional asymptotic analysis as well as a transient higher order asymptotic analysis.[7] The agreement obtained between CGS data and the higher order asymptotic analysis emphasized that contributions of the non-singular terms to the total stress and deformation fields are too important to be generally ignored.

Following the demonstration of feasibility of CGS to study fracture problems, a detailed Fourier optical analysis for the interferometer based on Fresnel diffraction theory was provided by the author.[3] In that work, light waves, represented as complex amplitudes passing through various optical elements of the CGS set up leading to the formation of interference fringes as perturbations of the initial planar object wave front, were analyzed and the validity of the earlier first-order diffraction analysis was demonstrated. The sensitivity analyses were carried out by Bruck and Rosakis[8] for transmission CGS in the study of mode-I cracks. They interpreted fringe data as gradients (geometric interpretation) and finite differences (physical interpretation) of hydrostatic stress fields. Their results showed that increasing the sensitivity of CGS improved both the quantity and quality of fringe data. The results also indicated that the apparent size of the region on the image plane affected by crack tip triaxiality increased as measurement sensitivity was increased. This in turn increased the differences between the geometric and physical interpretations of CGS fringe data.

Not too long after the initial success of CGS to study mode-I crack problems in transmission and reflection modes, the possibility of using CGS for mixed-mode fracture investigation of homogeneous solids was explored. A modified edge cracked Plexiglas beam with a horizontal edge crack subjected to three-point bending was used in Ref. [3] to demonstrate transmission CGS to generate mixed-mode (mode-I and -II) loading under static conditions. A mixed-mode fringe pattern from that work is shown in Fig. 10. The asymmetry of the fringes about the axis of the crack/notch is indicative of the mode-mixity (defined as $\tan^{-1}\frac{K_{II}}{K_I}$ where K_I and K_{II} are mode-I and -II stress intensity factors) in the local mechanical fields. The mixed-mode crack tip fields for the optical measurement are expressed as

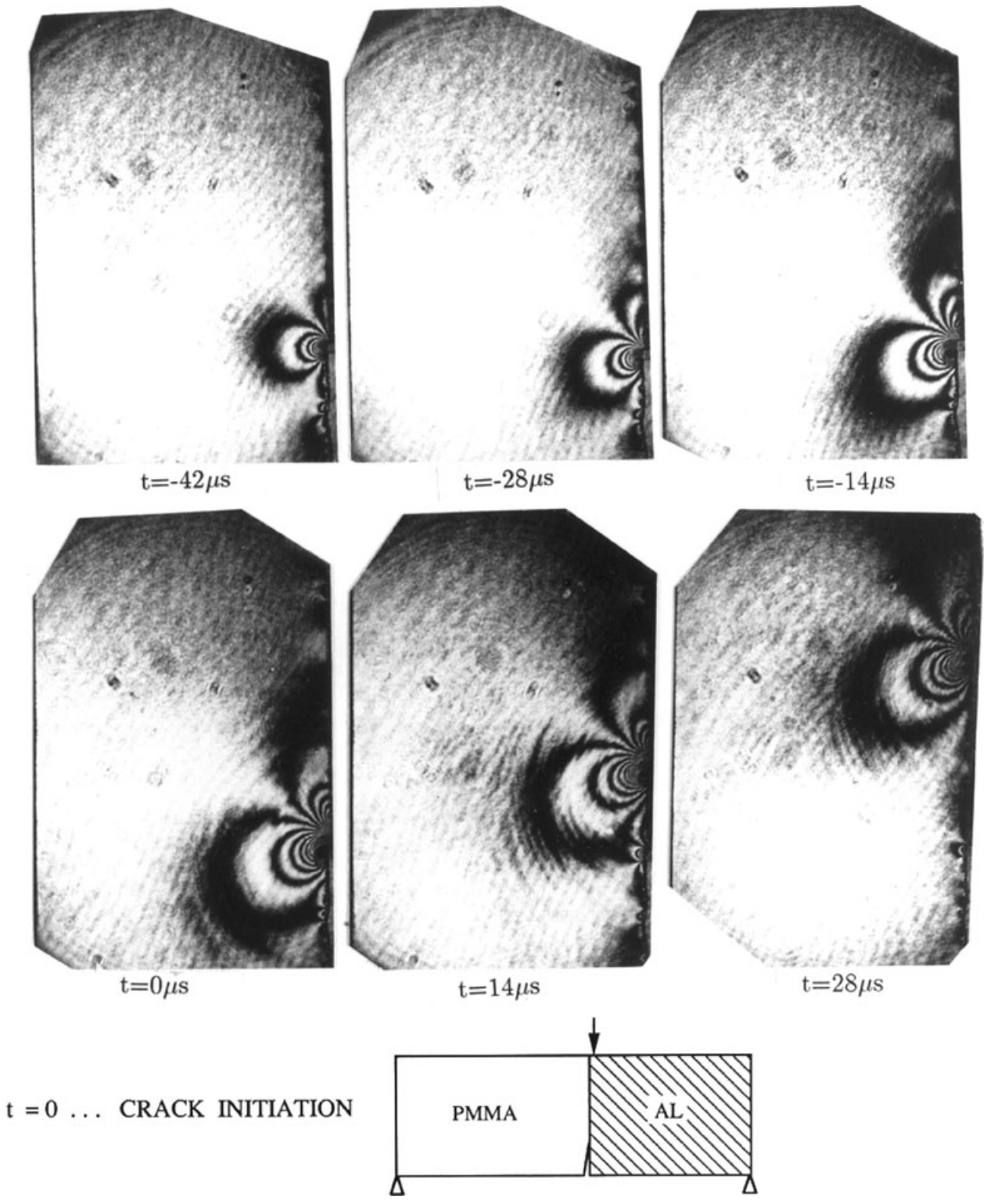

Fig. 13 Transmission-mode CGS interferograms representing fringes proportional to $\partial(\sigma_x + \sigma_y)/\partial x$ in the vicinity of a dynamically propagating interfacial crack in a PMMA/aluminum bimaterial. Fringes are visible only in the PMMA-half of the biomaterial.[24]

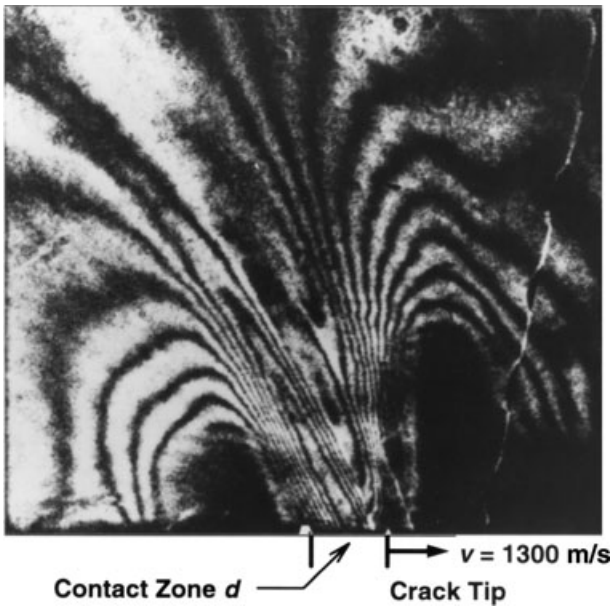

Fig. 14 Enlarged view of transmission-mode CGS fringes in the intersonic crack growth regime showing occurrence of crack face contact. Here the crack is growing from left to right along a PMMA/steel interface. Fringes are visible only in the PMMA (upper) half of the biomaterial. (Ref. [32], Courtesy A. J. Rosakis.)

$$C_\sigma B\left(\frac{\partial(\sigma_x+\sigma_y)}{\partial x}\right) = C_\sigma B\left(\frac{N}{2}-1\right) r^{\left(\frac{N}{2}-2\right)} \times\left[\sum_{N=1}^{\infty} A_N \cos\left(\frac{N}{2}-2\right)\theta + B_N \sin\left(\frac{N}{2}-2\right)\theta\right] = M\frac{P}{\Delta}, \quad M=0,\pm1,\pm2,\ldots, \tag{10}$$

where A_N and B_N are the coefficients of the asymptotic expansion and other terms as defined earlier in Eq. (9). As before, the terms associated with $N = 1$ represent the two stress intensity factors. The work was subsequently extended by Ramaswamy *et al*.,[9] and Tippur and Ramaswamy[10] using a different flexural geometry to generate a wide range of mode-mixities ranging from 20° to 65°. They also verified their measurements relative to analytical predictions based on flexural analysis of cracked beams.

The dynamic mixed-mode fracture behaviour of homogeneous solids was first explored by Mason *et al*.[11] They used transmission CGS apparatus to study a specimen geometry mimicking uniform pressure pulse imposed on the edge of a sheet with an edge crack (see Fig. 11). The choice of the loading geometry was motivated by the theoretical and numerical solutions for the problem of a crack in a semi-infinite elastic sheet under the action of a suddenly imposed uniform pressure pulse, reported by Lee and Freund.[12] In the experiments, the pressure pulse was generated using a flat rectangular punch attached to the falling weight of a drop-tower impacting an edge notched PMMA sheet along the edge adjacent to a pre-notch. The recorded optical patterns obtained using high-speed photography and pulsed laser light showed the evolution of dominant mode-II fringe patterns at the initial stages of loading followed by a time period during which fringe patterns transitioned to mixed-mode conditions, eventually becoming a dominant mode-I crack tip field before fracture initiated. The measured mode-I and -II dynamic stress intensity factor histories using least-squares analysis of the optical data were shown to closely match the predicted results. This work led Rosakis and co-workers[13,14] to investigate dynamic failure mode transition in C300 maraging steels using reflection CGS. Kalthoff and co-workers[15] had previously demonstrated that a crack subjected to dominant shear impact caused a failure mode-transition at a critical impact velocity. That is, below the critical impact velocity the crack path was dictated by conventional fracture mechanics theories whereas shear band formation occurred above the threshold value. Guduru *et al*.[14] were able to successfully capture surface slopes near a shear band generated from the tip of a fatigue crack subjected to shear dominant impact loading. A sequence of CGS interferograms from their experiment is shown in Fig. 12 along with the loading geometry used. In this work, thermal fields generated by the adiabatic deformations were also mapped simultaneously using a high-speed thermal imaging system. By combining optically measured stress intensity factors and thermal field measurements, they were able to make several new observations pertaining to shear band formation in steels. Among them, a critical range of K_{II} values for shear band initiation from a crack tip was identified.

Another report by Anderson and Rosakis16 used reflection CGS to study loading rate effects in 6Al-4V titanium alloys. They compared optically determined stress intensity factors with the ones from strain gages and crack tip opening displacements. They were able to quantify a significant drop in stress intensity factor (K_{I-cr}) at crack initiation with increasing loading rate characterized by $\dot{K}_I$[17] (because most materials show an increasing K_{I-cr} with increasing $\dot{K}_I$, these results with an opposite trend for Ti alloys emphasized the need for dynamic fracture testing of materials). More recently, Yao *et al*.,[18] have used transmission CGS to study local deformation fields near V-notches of various included angles from 0° to 150° in PMMA beams. They compared their optical contours with finite element computations for the same geometry successfully.

Interfacial fracture mechanics

A major contribution of CGS to fracture mechanics has been in the area of interfacial crack growth. Although foundation for interfacial fracture mechanics was laid some 20 years earlier (see, e.g. Refs [19–22]), advances in engineering composites and electronic devices rejuvenated interfacial fracture mechanics activity in the late 1980s. Until then only a few optical investigations[23] had been published on this topic. By taking advantage of its ability to investigate fracture problems effectively, CGS was extended to interfacial fracture mechanics study by Tippur and Rosakis.[24] They studied a bimaterial beam made of equal thickness sheets of PMMA and aluminium bonded along a straight interface (elastic mismatch or oscillatory index $\varepsilon = 0.098$). A strong bond was created by roughening the aluminium half and using an adhesive made of methyl methacrylate monomer to avoid a distinctly different third material. The bimaterial beam was optically examined using transmission CGS resulting in crack tip interferograms only on the polymer half of the bimaterial. Using the characteristic oscillating singularity solution involving leading terms for hydrostatic stress gradient

$$C_\sigma B\left(\frac{\partial(\sigma_x+\sigma_y)}{\partial x}\right) = C_\sigma B r^{-3/2}\frac{\exp[\varepsilon(\theta-\pi)]}{\sqrt{2\pi}\cosh(\pi\varepsilon)} \times \begin{pmatrix} -Q_1\cos\left(\frac{3\theta}{2}+\varepsilon\ln\frac{r}{a}\right) - 2\varepsilon Q_1\sin\left(\frac{3\theta}{2}+\varepsilon\ln\frac{r}{a}\right) \\ +Q_2\sin\left(\frac{3\theta}{2}+\varepsilon\ln\frac{r}{a}\right) - 2\varepsilon Q_1\cos\left(\frac{3\theta}{2}+\varepsilon\ln\frac{r}{a}\right) \end{pmatrix} = M\frac{P}{\Delta}, \quad M = 0, \pm1, \pm2, \ldots \tag{11}$$

they were able to successfully extract the magnitude of the complex stress intensity factor $K = (K_1 + iK_2)$. In the aforementioned expression ε denotes the elastic mismatch index and Q_1 and Q_2 are related to the magnitude of the stress intensity factor as $|K| = |K_1 + iK_2| = \sqrt{Q_1^2 + Q_2^2}$. The discrepancies they observed regarding the phase angle (defined as $\Psi = \tan^{-1}(Q_2/Q_1)$ using $Q_1 = |K|\cos\psi$ and $Q_2 = |K|\sin\psi$) suggested the need for employing higher order terms of the asymptotic stress fields. Another lasting contribution of this work was in the area of dynamic decohesion of coherent interfaces. In fact, until its publication there were no reports on photomechanics investigation of dynamic crack growth along dissimilar material interfaces despite a need for understanding failure behaviour of layered materials and composite structures under impact loading. In this ground-breaking optical investigation, Tippur and Rosakis[24] observed unusually high crack speeds during dynamic fracture of bimaterial specimens subjected to low-velocity impact. They studied the same bimaterial beam used in their static tests using transmission CGS and high-speed photography (140,000 frames per second). The bimaterial specimen with an edge notch along the interface was impact loaded on the aluminium half (velocity 2 m/sec) close to the interface using a drop-tower in a three-point bend configuration. A record of angular deflections of light rays in the interfacial crack tip vicinity in the PMMA half they obtained is shown in Fig. 13. In this sequence of interferograms, time instants shown correspond to times before (negative) and after (positive) crack initiation. The dynamic effects are clearly visible as sharp kinks in otherwise smooth fringes. Also, rotation of fringe lobes before crack initiation suggests changing shear to normal stress ratios at the crack tip with the passage of time. Initially the crack tip experiences dominant shear deformations due to higher elastic wave speeds in the aluminium half relative to the PMMA half. At later time stress waves returning from the far boundaries increase the tensile stresses at the crack tip until crack initiation. In the post-initiation period, the crack tip fringes seem relatively self-similar. These interferograms were used to record the instantaneous crack tip location and the crack velocity history was deduced. Surprisingly high crack velocities, approaching 80% of the Rayleigh wave speed of the compliant constituent (PMMA) of the bimaterial, was recorded. At the time of this research, there were only a few theoretical studies on this topic[25–28] and explicit crack tip field equations to extract fracture parameters, such as stress intensity factors, mode-mixity and energy release rate were absent. Additionally, there were disagreements on issues related to terminal interfacial crack speeds. For example, the results of Willis[27] differed from that of Atkinson[28] regarding the terminal velocity. The former claimed that the terminal velocity of an interfacial crack to be slightly greater than the lower of the two Rayleigh wave speeds of the constituents whereas the latter suggested it to be equal to the lower of the two Rayleigh wave speeds.

Tippur and Rosakis'[24] experiments inspired several follow-up theoretical, numerical and experimental works on interfacial fracture of bimaterials. Yang *et al*.,[29] developed instantaneous field equations for a steadily propagating interfacial crack. The sum of the two in-plane normal stresses from their analysis are given by

$$(\sigma_x+\sigma_y) = \frac{A(t)}{\sqrt{2\pi r_1}}\left[\begin{array}{l} \left(1+\alpha_x^2-2\eta\alpha_s\right)\exp\{\varepsilon(\pi-\theta_l)\}\cos\left(\frac{\theta_l}{2}-\Phi(t)-\varepsilon\ln r_l\right) \\ +\left(1+\alpha_x^2+2\eta\alpha_s\right)\exp\{-\varepsilon(\pi-\theta_l)\}\cos\left(\frac{\theta_l}{2}-\Phi(t)+\varepsilon\ln r_l\right) \end{array}\right], \tag{12}$$

where

$$A(t) = \frac{\left(\alpha_l^2 - \alpha_s^2\right)|K^d(t)|}{D(v)\cosh(\pi\varepsilon)}, \quad K^d(t) = K_1^d(t) + iK_2^d(t)$$

$$\Phi(t) = \tan^{-1}\frac{K_2^d(t)}{K_1^d(t)},$$

and $\alpha_{l,s}$ are functions of crack tip velocity, longitudinal and shear wave speeds of the material and K^d is the complex dynamic stress intensity factor expressed in terms of its components K_1^d and K_2^d. The variables $(r_{l,s}, \theta_{l,s})$ represent contracted polar coordinates which account for the rapidly growing crack and elastic mismatch parameter $\varepsilon(\equiv\varepsilon(v))$ as well as D and η are functions of crack speed. These steady-state crack growth results were subsequently enriched by a detailed transient analysis of a dynamically propagating interfacial crack by Liu *et al*.[30,31] An important conclusion of the new theoretical analyses was that as the crack tip approached the lower of the two Rayleigh wave speeds of a bimaterial, a finite amount of energy was required for the crack tip to maintain propagation at the Rayleigh wave speed with a non-zero complex stress intensity factor. This observation was unlike the ones for homogeneous counterparts that required infinite energy to maintain crack propagation at the Rayleigh wave speed.[30,31] Thus, the restriction for the crack to extend along the interface at speeds in excess of the Rayleigh wave speed was absent in a bimaterial. An experimental evidence for this was reported by Lambros and Rosakis[32] who conducted an optical investigation on PMMA-steel bimaterials using transmission CGS. In their experiments a gas-gun (instead of a drop-tower used earlier in Ref. [24]) was used for impacting the specimens at substantially higher velocities. The resulting interferograms were used to track crack growth history as well as map crack tip deformations. By analyzing the interferograms they demonstrated the need for a transient higher order crack tip field description instead of a steady-state K-dominant description[29] to capture the local behaviour satisfactorily. Their measurements revealed that interfacial crack speed exceeded not only the Rayleigh wave speed for PMMA but its shear wave speed as well. In a set of experiments when a blunt interfacial notch (capable of storing significant amounts of strain energy prior to initiation) was used, they reported crack speeds approaching the longitudinal wave speed of PMMA and demonstrated the possibility of interfacial crack propagation at intersonic (between shear and longitudinal wave speeds) speeds. They were also able to provide visual evidence of crack propagation in the intersonic regime. By comparing CGS fringes at early stages of propagation with the ones at intersonic speeds, they observed the main fringe lobes (ahead of the crack tip) to have a squeezed appearance in the crack growth direction along with 'shock-like' discontinuities. The crack propagation in the intersonic regime also revealed certain special features. In the subsonic range the interfacial crack showed evidence of fringe lobes coming to focus at a single point along the interface, the apparent crack tip. When the crack attained intersonic speeds, however, the rear and front lobes intercepted the interface over a finite length without a common focus suggesting large-scale crack face contact. This can be seen in a transmission CGS interferogram (in the PMMA half above the bimaterial interface) from that work shown in Fig. 14 where the length between the front and rear lobes is marked by the letter d. (Even though crack propagation occurred at speeds in excess of shear wave speeds, they could not visualize the shear stress discontinuity because transmission CGS measurements were proportional to $(\sigma_x + \sigma_y)$. This necessitated the use of photoelasticity by Rosakis and coworkers, subsequently.) As interfacial crack tip field expressions had become available by that time, estimation of relevant complex stress intensity factor histories (and hence energy release rate and mode-mixity) from interferograms using over-deterministic least-squares analysis of optical data were carried out by the authors. The energy release rate (G) history showed a highly unstable crack initiation event resulting in a steep drop in G values during the time period when crack accelerated to intersonic speeds after initiation. During the same time period, the mode-mixity continued to increase rapidly. They also noted that during interfacial crack growth crack tip opening angle remained constant.

A few other interfacial fracture mechanics studies aided by transmission CGS have also been reported in the intervening years. A modified flexural geometry proposed by Ramaswamy *et al*.,[9] to study mixed-mode fracture of homogeneous materials was extended by Ramaswamy and Tippur[10] to bimaterials. They studied bimaterials with a large elastic mismatch made of PMMA and aluminium beams with cracks along the interface under quasi-static loading. They were able to achieve a crack tip mode-mixity of approximately –50° to –10° (with crack length as the scaling parameter) using this specimen geometry. Their measurements compared well with analytical results based on flexural analysis of bimaterial beams. They were also able to establish a critical energy release rate versus mode-mixity map for this bimaterial system using their optical measurements. In a subsequent work, Xu and Tippur[33] employed single edge cracked asymmetric four-point bend geometry for the same bimaterial system. They also used transmission CGS to measure crack tip fringes and deduce mode-mixity for various off-set loading distances relative to the interface. A much larger range of mode-mixities, between –75° and +90° with 1 mm as the length scaling parameter, were achieved and a critical energy release rate versus mode-mixity map was produced. A fourfold variation between the lowest and the highest

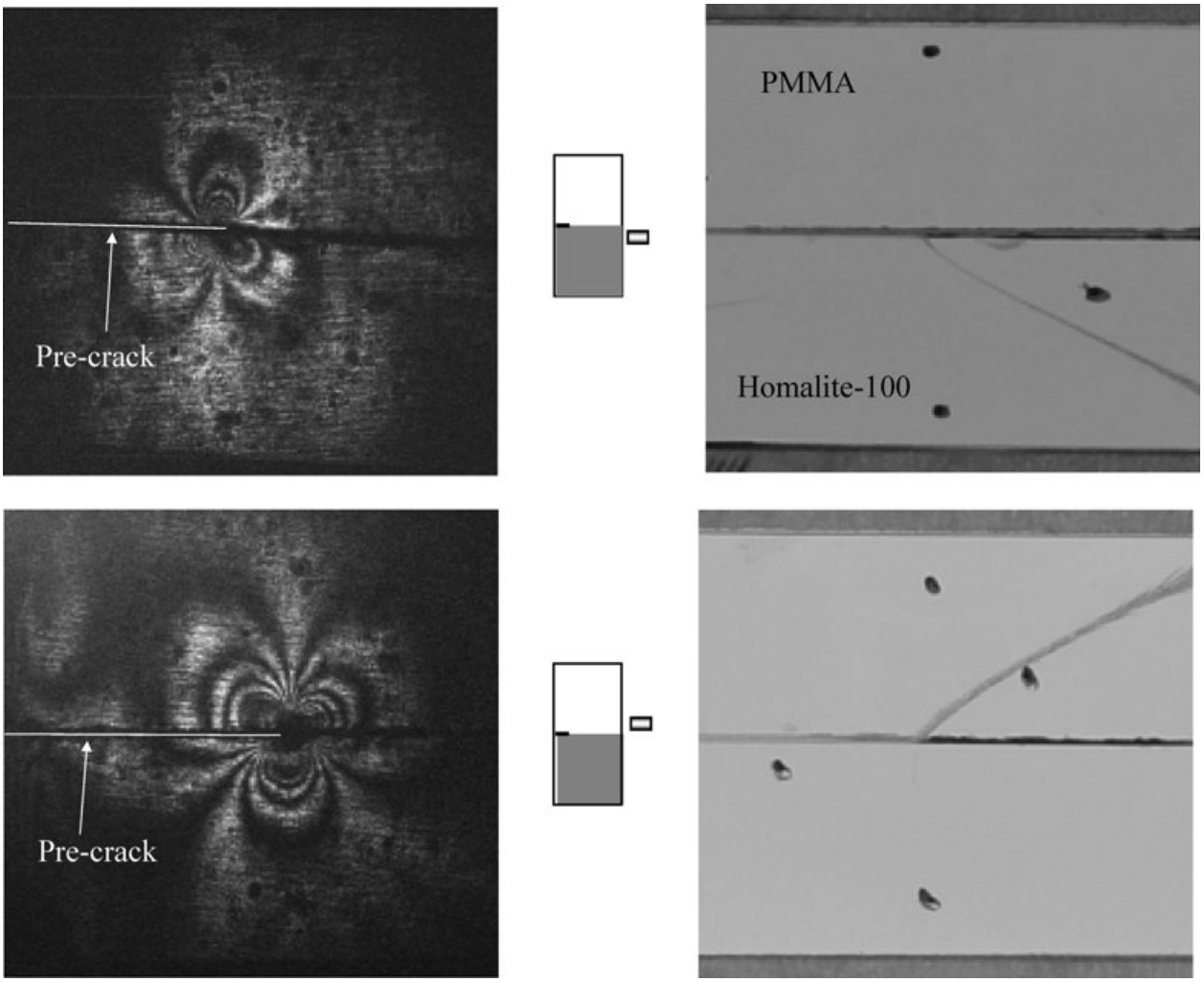

Fig. 15 Transmission CGS interferograms at crack initiation (left) and *post mortem* optical photographs (right) of two selected dynamic tests yielding different initiation mode mixities. The loading configuration used in each case is schematically shown in the centre of the figures, which correspond to $\delta_r = -25$ mm (top row), $\delta_r = +25$ mm (bottom row). (Ref. [35], Courtesy J. Lambros.)

value of critical energy release rate was reported. Further a large difference in crack initiation fracture toughness at large negative and positive mode-mixities was also observed. They also studied the role of surface roughness on the apparent fracture toughness of interfaces. These authors[34] also undertook dynamic fracture study of PMMA-aluminium bimaterial interfaces using transmission CGS and high-speed photography in order to establish crack initiation toughness as a function of mode-mixity under stress-wave loading conditions.

Kimberley and Lambros[35] used transmission CGS and high-speed photography to study interfacial crack kinking phenomenon in bimaterial panels subjected to impact loading. They examined PMMA and Homalite-100 bimaterial (elastic mismatch index $\varepsilon = 0.0028$) panels bonded along a straight interface and impact loaded at various locations on edges behind or in front of a pre-notch along the interface using a gas gun. The optical transparency of both halves of the bimaterial yielded interferograms in the upper as well as the lower halves of the specimen (see Fig. 15). By varying the impact location, they were able to generate and optically quantify a wide range of mode-mixities and complex stress intensity factors at crack initiation by analyzing the CGS fringes. By coupling the optical measurements with measured crack kink angles from fractured specimens, a crack kinking criteria for bimaterials was suggested. They concluded that the maximum opening stress or maximum energy release rate criteria based on quasi-static crack tip fields was sufficient to capture crack kinking behaviour for dynamic loading as well when elastic mismatch between the two halves of the bimaterial is small.

Particulate composites

CGS has been used in a few recent investigations to examine the dynamic fracture behaviour of composites with particulate reinforcements. Due to the opacity of particulate composites, these studies employed reflection CGS technique. The effect of filler particle size on the mode-I fracture behaviour of glass-filled epoxy was studied by Kitey and Tippur.[36] They examined composites made of 10% volume fraction of spherical glass beads of different average size in the range of 11–200 μm dispersed uniformly in epoxy. They also considered adhesion strength between reinforcement and matrix as a parameter. The sample surfaces were aluminized (see Fig. 2) to make the crack tip region amenable to reflection CGS and high-speed photography. Edge cracked beams subjected to symmetric one-point impact loading were used to propagate mode-I cracks dynamically and map surface slopes near the growing crack tip. Using high-speed imaging and least-squares analysis of fringe data they quantified crack speed, stress intensity factor at crack initiation, and during steady growth as a function of average filler particle size. A significant particle size effect on fracture toughness (both crack initiation and steady-state growth values) in case of composites with weakly bonded reinforcements was reported. Their experiments also revealed an optimum mean particle size of ~35 μm for which fracture toughness values were the highest. That is, fracture toughness decreased as particle size increased or decreased relative to this particle size. The maximum crack speed also increased as particle size decreased for weakly bonded reinforcements. The steady-state crack speed showed an inverse relationship with the steady-state fracture toughness. The results also showed that particle size had a negligible effect on fracture toughness values when filler particles were strongly bonded to the matrix. Furthermore, steady-state fracture toughness values for all reinforcement sizes were consistently lower than the corresponding ones for composites with weakly bonded filler, a rather counterintuitive result.

The dynamic fracture studies on particle reinforced epoxy composites motivated Kitey and Tippur[37] to visualize how a dynamically growing crack in a matrix interacts with a stationary stiff inclusion. They investigated this problem in a 2D setting using cylindrical glass inclusion positioned in the prospective crack path in a brittle epoxy sheet. They again employed reflection CGS and high-speed photography to record surface slopes near a rapidly growing crack as it initiated from a pre-notch in a beam subjected to impact loading. Strongly and weakly bonded inclusions at different off-set distances between the inclusion centre and the crack line (eccentricity denoted as e) were studied (see Fig. 16). Distinctly different crack trajectories were seen when the inclusion was

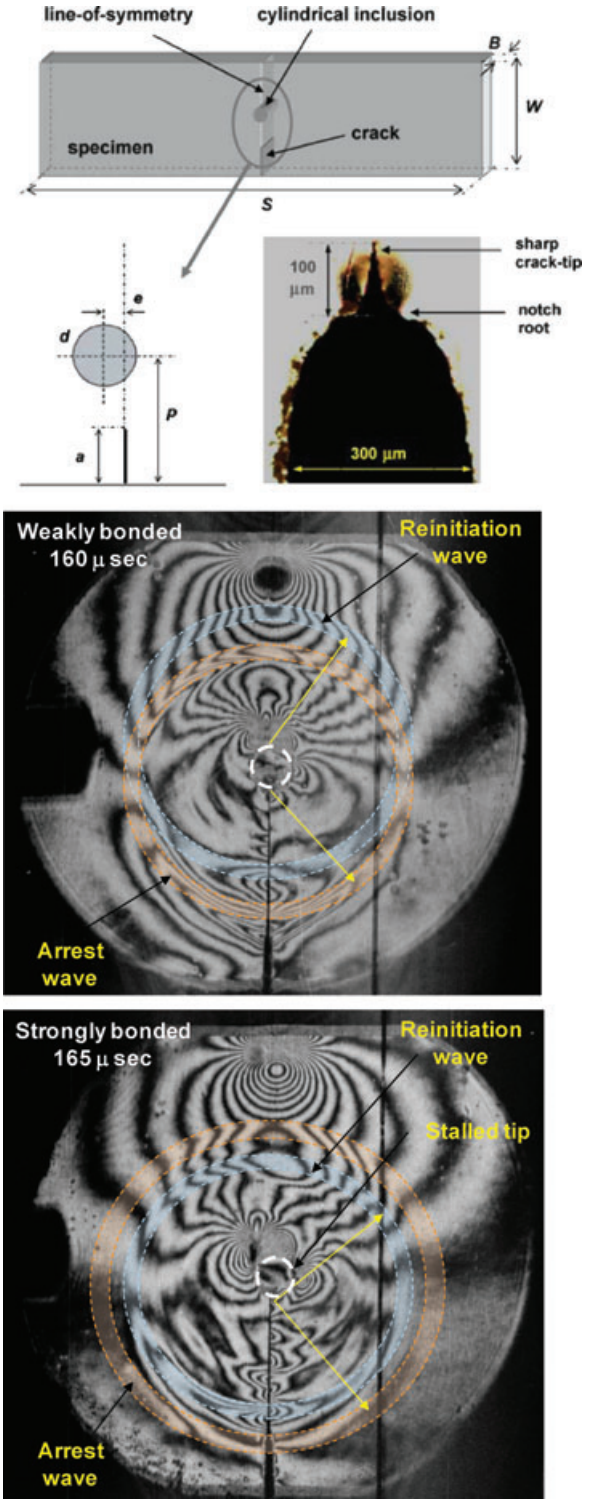

Fig. 16 Crack-inclusion geometry ($e = 0$) used to study dynamic crack growth past a stiff inclusion in a matrix. Reflection CGS interferograms at time instants when crack arrest and reinitiation occur in samples with weakly bonded and strongly bonded inclusion. The vertical line parallel to the initial notch is 10 mm away from the crack line.[37]

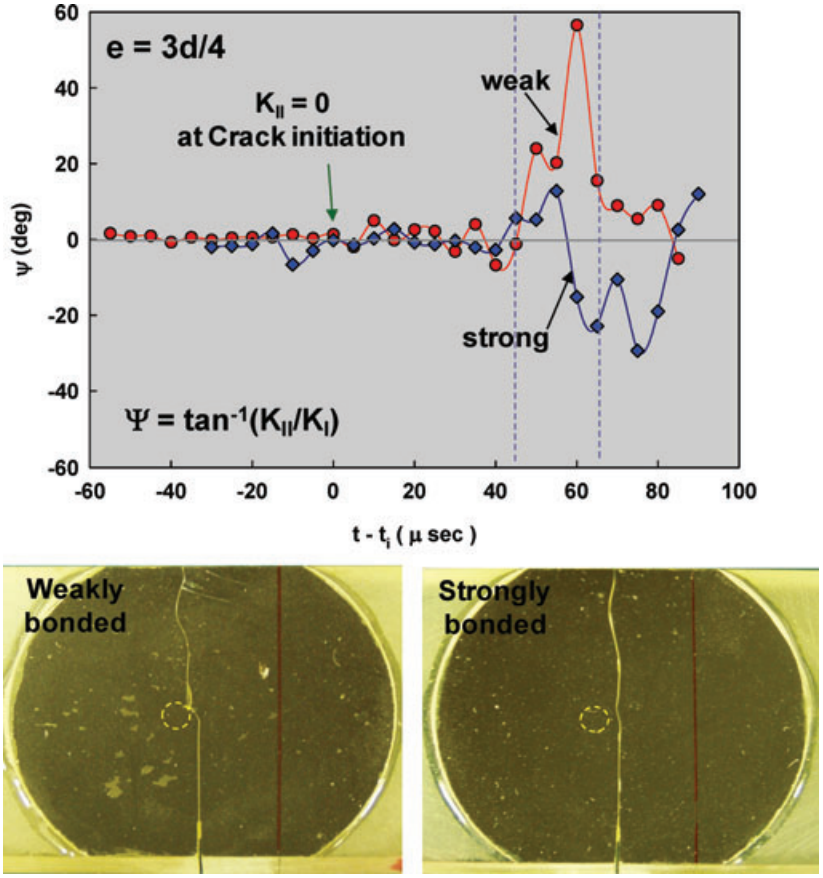

Fig. 17 Variation of mode-mixity for weakly and strongly bonded inclusions (eccentricity $e = 3d/4$). Crack attraction and deflection can be readily seen in fracture samples and confirmed by positive and negative mode-mixities measured using reflection CGS.[37]

bonded strongly or weakly to the matrix. They noted that a weaker inclusion-matrix interface attracted a propagating crack whereas a stronger interface deflected the crack away. Multiple stress waves observed from the CGS interferograms (see Fig. 16) as the crack interacted with the inclusion were used to understand the failure process. The optical trace of the stress waves associated with crack arrest and reinitiation were concentric for the strongly bonded inclusion suggesting both to have originated from relatively close spatial positions near the interface with a time delay between arrest and reinitiation. On the other hand, the trace of the same two waves were seen as two nearly equal intersecting circles as they originated from two different spatial locations on the interface due to spontaneous debonding of the weak inclusion-matrix interface. Also, for the crack propagating towards a weakly bonded inclusion, the effective stress intensity factor (K_e) attained a constant value and then dropped when the crack tip was very close to the inclusion or lodged into inclusion-matrix interface. In the strongly bonded inclusion cases, however, K_e increased monotonically as the crack propagated towards the inclusion. The opposite signs of crack tip mode-mixities (see Fig. 17) near the inclusion further substantiated crack attraction and repulsion behaviour of a crack propagating towards inclusion-matrix interface in weakly and strongly bonded inclusion cases, respectively.

Functionally graded materials

Since the early nineties there has been a growing interest in a family of bio-inspired materials called functionally graded materials (FGM). FGMs are macroscopically isotropic but non-homogeneous materials with continuously varying material properties along one or more spatial directions. These novel materials were initially proposed for mitigating deleterious effects of discrete interfaces encountered in traditional layered materials and composite structures in extreme loading environments. The gradual variation of material properties in FGMs are generally achieved using composite architectures in which volume fractions of individual constituents are spatially varied. In a particulate metal-ceramic composite FGM,[38] for example, the variation could be from 100% metal at one end to 100% ceramic at the other in a continuous manner. The mechanical characterisation in general and fracture behaviour in particular is at the heart of understanding mechanical integrity such novel materials. Investigating the fracture behaviour of FGMs using optical methods has been part of this broader endeavour.

CGS has contributed to the understanding of fracture mechanics of FGMs. Tippur and co-workers,[39–45] examined the influence of continuous compositional gradients on the fracture response of functionally graded composites using reflection CGS. They studied glass-filled epoxy composite sheets with continuously varying filler volume fraction. The FGM they developed was made from either solid glass microspheres (35 and 42 μm average diameter) or hollow glass microballoons (60 μm average diameter and ~0.5 μm wall thickness) as filler materials in epoxy matrix. The former FGM was a non-homogeneous material with a monotonic unidirectional volume fraction variation of solid filler particles from approximately 0 to 40% over a length of approximately 45 mm. In the latter, a similar volume fraction variation was achieved using hollow microballoons resulting in lightweight syntactic structural foam with closed-cell porosity. While solid glass spheres increased the stiffness continuously, the hollow microballoons decreased the same in the FGM. Due to the opacity of these non-homogeneous materials, the specimens were made optically reflective for implementing CGS using the method detailed earlier. Butcher *et al*.,[39] compared quasi-static fracture parameters of a bimaterial beam with a sharp interface and the one with a linearly graded architecture (with an approximately linear variation in Young's modulus normal to the crack orientation). Their measurements favoured the graded architecture in terms of failure response. The asymmetry of interferograms also indicated mixed-mode deformation of the crack tip and led to an investigation[40] of fracture response as the location of the crack in the graded region of the beam was varied. They noted that fracture performance of FGM in terms G/G_{cr} (G and G_{cr} being energy release rate and measured fracture toughness, respectively) were consistently better than the corresponding bimaterial counterparts. They also examined crack kinking for different crack locations within the graded region and noted that the *initial* kink angle in FGMs matched those based on maximum tangential stress theory used for homogeneous brittle solids. In a separate study on edge cracked glass-filled epoxy functionally graded beams, Rousseau and Tippur[42] examined crack tip stress fields using CGS when the elastic gradient was along the crack direction. The optical measurements revealed that for a crack on the compliant side of the FGM beam to have a significantly lower stress intensification (by a factor of ~1.5) when compared to the one with a crack on the stiff side. They also measured crack tip stress intensity factors to an accuracy of 10–20% relative to the analytical results by assuming a locally homogeneous crack tip field. Rousseau[46] later on re-visited these results but using crack tip stress field expressions which account for non-homogeneity of the material. He was able to improve the accuracy of stress intensity factor determination significantly.

First optical investigation of dynamic fracture of FGM with continuous variation of properties used reflection CGS. Rousseau and Tippur[41] studied mode-I dynamic crack growth along the compositional gradient in functionally graded beams subjected to one-point impact using CGS and high-speed photography. Their optical measurements revealed strikingly different post-crack initiation stress intensity factor histories and crack growth resistance behaviours in glass-filled epoxy FGMs with monotonically increasing and decreasing compositional gradients. They analyzed the CGS fringes using expression for instantaneous steady-state crack tip out-of-plane displacements[47] for non-homogeneous materials,

$$w(t) = \frac{-\nu B}{2(1+\nu)(1-2\nu)} \left\{ A_0(t) r_l^{-\frac{1}{2}} \cos\frac{\theta_l}{2} + A_1(t) + A_2(t) r_l^{\frac{1}{2}} \cos\frac{\theta_l}{2} - \frac{\alpha}{4\alpha_l^2} A_0(t) r_l^{-\frac{1}{2}} \cos\frac{3\theta_l}{2} + \frac{2\alpha\alpha_s}{(k+2)\left(\alpha_l^2-\alpha_s^2\right)} B_0(t) r_s^{\frac{1}{2}} \cos\frac{\theta_s}{2} \right\}, \tag{13}$$

where

$$k = \frac{\lambda_0}{\mu_0}, \quad \alpha_l = \sqrt{1 - \frac{\rho_o c^2}{\mu_0(k+2)}}, \quad \alpha_s = \sqrt{1 - \frac{\rho_o c^2}{\mu_0}},$$

$$r_{l,s} = \sqrt{x^2 + \alpha_{l,s}^2 y^2}, \quad \theta_{l,s} = \tan^{-1}\frac{\alpha_{l,s} y}{x},$$

$$A_0 = \frac{\left(1+\alpha_s^2\right)\left(1-\alpha_l^2\right)}{4\alpha_s\alpha_l - \left(1+\alpha_s^2\right)^2} \frac{K_{ID}}{\mu_c\sqrt{2\pi}}, \quad B_0 = \frac{2\alpha_l}{1+\alpha_s^2}\frac{1-\alpha_s^2}{1-\alpha_l^2} A_0.$$

In the aforementioned equations, λ is Lamé's constant, $\mu_c = \mu_o \exp(\alpha c t)$ where α the non-homogeneity parameter and c is the crack speed. The coefficients A_0, A_1 and A_2 are unknown coefficients of the asymptotic expression. Evidently, as the material gradient parameter α becomes zero, the equations reduce to that of its homogeneous counterpart. A continuous increase in the dynamic stress intensity factors occurred when the crack propagated into a region of progressively increasing filler volume fraction while an opposite trend was observed in the case with an opposite compositional gradient ahead of the growing crack. They attributed these differences to a combination of stiffness and fracture toughness gradients in FGMs.

Reflection CGS was also used to study mixed-mode dynamic fracture of unidirectionally graded FGM beams by Kirugulige and Tippur.[48,49] In their work, differences in fracture behaviour in terms of crack initiation time, crack path, crack speed and stress intensity factor histories were evaluated optically in glass-filled epoxy beams. Two FGM configurations, one with a crack on the compliant and the other with a crack on the stiff side, were studied under one-point impact applied eccentrically relative to the crack plane, as shown in Fig. 18. (The variations in

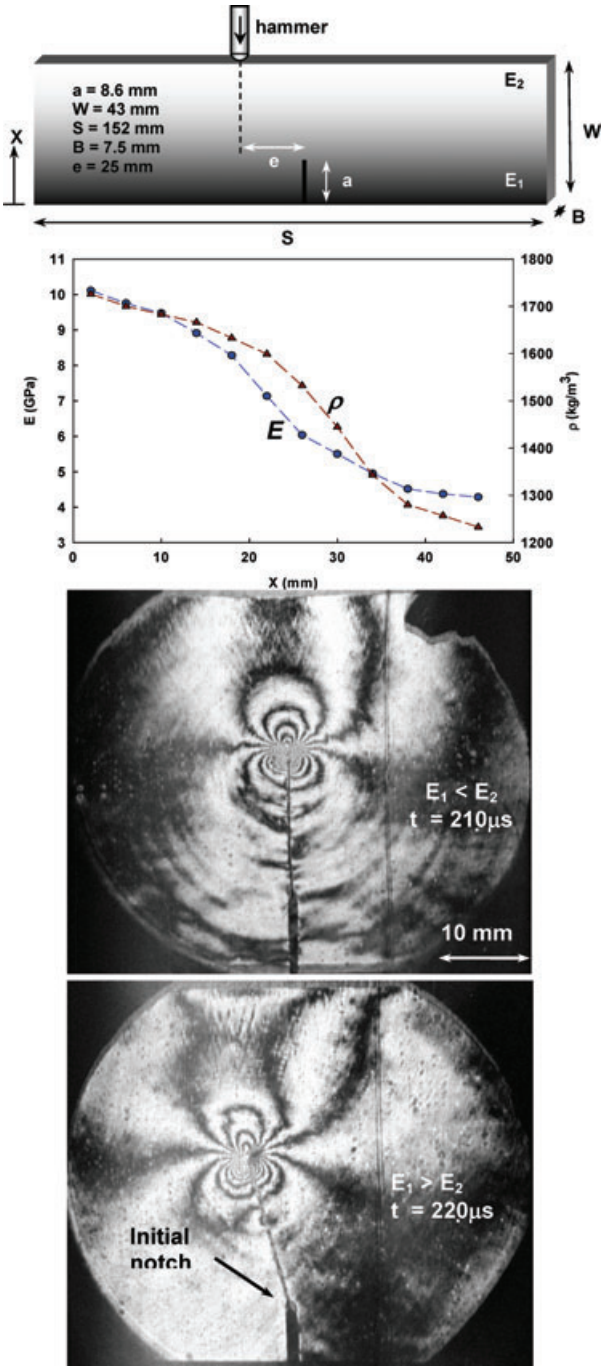

Fig. 18 Fringe patterns representing surface slopes dw/dx (w being out-of-plane displacement) near dynamically propagating cracks in FGM subjected to impact loading as shown in the schematic. The elastic (E) and mass density (ρ) variations in the vertical direction are shown in the plot. Distinctly different crack paths are obtained depending upon the compositional gradient ($E_1/E_2 \sim 0.4$ in the top and ~ 2.5 in the bottom reflection CGS interferograms).[48]

the Young's modulus and mass density over the width of the sample are also shown in Fig. 18.) Two representative optical interferograms from this investigation are shown in this figure. The images on the top and the bottom, respectively, are for two different situations when the initial crack was located at the edge of the specimen with a lower ($E_1 < E_2$) and a higher ($E_1 > E_2$) volume fraction of filler particles compared to the edge where the impact occurred. As evident from the interferograms, the crack paths in these images were strikingly different. The crack path in the $E_1 < E_2$ case was nearly self-similar even though the crack tip was subjected to combined mode-I and -II loading (by eccentric impact) whereas in the $E_1 > E_2$ case the crack kinked from the initial tip and grew at an angle relative to the pre-notch. The loading configuration and the sample geometries of the specimens studied being identical in these two cases, the differences in crack paths were attributed to a combination of elastic and fracture toughness gradients present in the two FGM configurations. Using over-deterministic least-squares analyses of interferograms corresponding to different time instants after impact, a history of stress intensity factors $K_I(t)$ and $K_{II}(t)$ and mode-mixities $\psi(t) = \tan^{-1}\frac{K_{II}}{K_I}$ were evaluated. Just prior to crack initiation, $\psi(t)$ values approached zero suggesting failure initiation under predominantly mode-I conditions. In the post-initiation period mode-mixity histories showed a small positive value of mixity in case of FGM with $E_1 < E_2$ whereas it was a small negative value in case of FGM with $E_1 > E_2$. Interestingly, the mixity history in the post-initiation period for the homogeneous sample remained close to zero in the window of observation, consistent with dynamic crack growth in homogeneous brittle solids. These results raised the possibility of a non-zero K_{II} during mixed-mode dynamic crack growth in brittle FGM.

In the past few years, CGS has also been found useful in the study of fracture behaviour of syntactic structural foams* by Tippur and his co-workers.[44,45] These authors have investigated static and dynamic fracture response of syntactic foam sheets with functionally graded porosity. Further, mechanics of fracture of these materials were studied in homogeneous, non-homogeneous and sandwich configurations. In case of monotonically graded foams subjected to symmetric one-point impact loading,[45] they reported that mode-I stress intensity factors increased when crack growth occurred from the compliant side to the stiffer whereas the opposite occurred when the growth was from the stiffer side to the compliant.

* Syntactic foams are lightweight structural foams made by dispersing *hollow* ceramic or polymeric microballoons into metal or polymer matrix materials resulting in a closed-cell microstructure. The porosity in these foams is typically microscopic unlike the conventional structural foams and is controlled by the volume fraction of the filler material in the matrix.

They attributed this to the reduction in fracture toughness with increasing microballoon volume fraction in the foam and the resulting differences in the in-plane crack tip constraint. For sandwich configurations with non-homogneous foam core (bilinear gradation with stiffer foam near the face-sheets and compliant foam in the middle), a suppression of face-core interfacial separation was observed during dynamic fracture experiments.

Fibre reinforced composites

CGS has been found to be a rather convenient tool in the study of fracture behaviour of fibre reinforced composites as well. At the moment there are only a few reports on the investigation of crack tip fields and fracture parameter measurement in these materials. Liu *et al*.,[50] examined the feasibility of reflection CGS to investigate crack tip fields in unidirectional graphite/epoxy composites. They represented surface slopes in the crack tip vicinity in a planar orthotropic solid with a crack oriented in the fibre direction using dominant terms as

$$\frac{\partial w}{\partial x} = \frac{B}{4\sqrt{2\pi}} r^{-3/2} \left(K_{\mathrm{I}} F_{xx}(\theta) + K_{\mathrm{II}} F_{xy}(\theta) \right) = N \frac{P}{2\Delta}, \quad N = 0, \pm 1, \pm 2, \ldots, \tag{13}$$

where w is the displacement in the out-of-plane directions and $F_{xx}(\theta)$ and $F_{xy}(\theta)$ are angular functions of θ as well as orthotropic material constants. (A detailed list of these angular functions can be found in Ref. 50.) Using least-squares analysis of interference data in conjunction with crack tip stress fields, they showed that the optically measured stress intensity factors agreed well with those obtained from direct load measurements and analytical predictions. They also quantified the crack initiation fracture toughness and crack growth resistance. Lambros and Rosakis[51] were the first to extend CGS to the study of fast-fracture in unidirectional graphite-epoxy composite plates. They studied symmetric one-point impact loading (impact velocity ~4 m/sec) geometry. The crack growth in their tests occurred under nominally mode-I conditions at speeds reaching nearly 50% of the Rayleigh wave speed (C_{R}). As a consequence of material anisotropy, an elliptical stress wave emanating from the initial notch triggered by crack initiation event was also observed. By analyzing fringes at crack initiation they estimated initiation toughness of the composite ($K_{\mathrm{Ii}} \sim 2.3$ MPa$\sqrt{\mathrm{m}}$). Unidirection graphite/epoxy composite sheets, IM7/8551–7, were also studied by Liu *et al*.,[52] under mode-I impact loading conditions. They used reflection CGS to capture fast fracture in specimens at a rate of 600,000 frames per second. A few interferograms from their experiment for crack growth along the fibres is shown in Fig. 19. Despite the high stiffness of the material, highly discernable

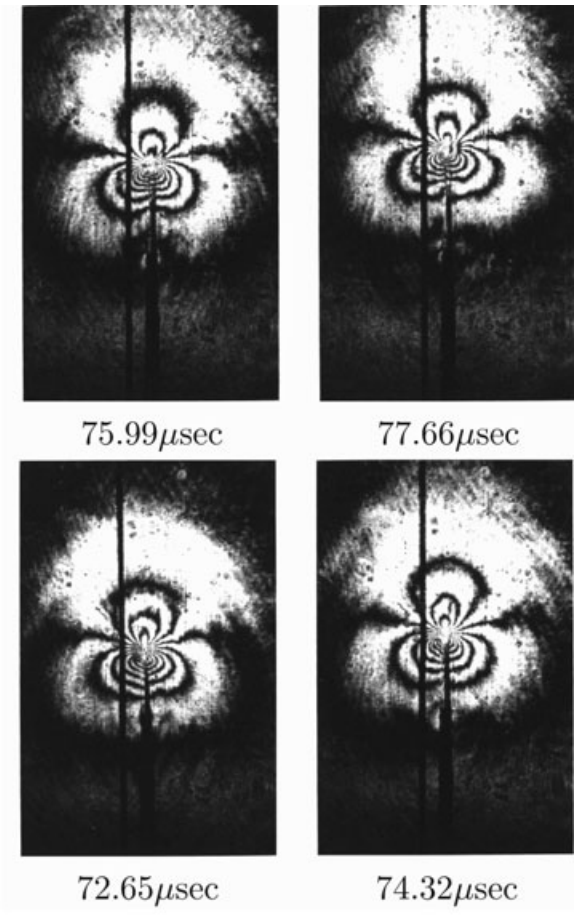

Fig. 19 Variation of fracture toughness with crack speed in unidirectional graphite/epoxy IM7/8551–7 composite measured using CGS. (Ref. [52], Courtesy C. Liu.)

fringes surround the propagating crack tip. The authors used interference patterns along with a newly developed stress-field expressions to extract energy release rate history. From the interferograms they also determined crack length history and deduced instantaneous crack velocities to be in the range of 500–2200 m/sec (1875 m/sec

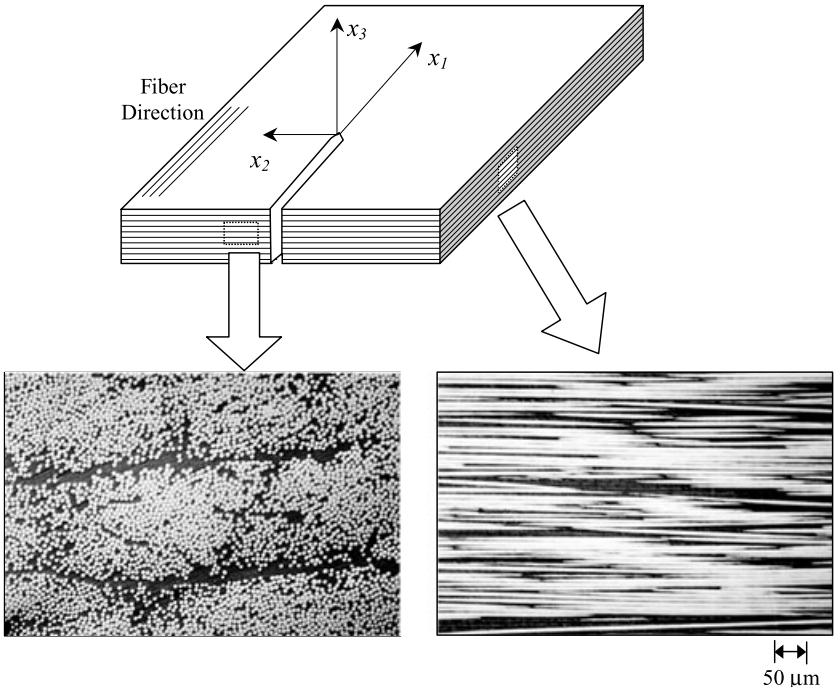

Elastic Properties		Characteristic Wave Speeds	
E_1	80 GPa	$c_l^{//}$	7500 m/s
E_2	8.9 GPa	$c_{\perp}$	2700 m/s
ν_{12}	0.25	c_s	1560 m/s
μ_{12}	3.6 GPa	c_R	1548 m/s

Fig. 20 Cross-sectional view of fibre-reinforced unidirectional graphite-epoxy composite and definition of the coordinate system with respect to the material symmetry axes. The table shows plane strain elastic characteristics of the composite. (Ref. [53], Courtsey A. J. Rosakis.)

being the shear wave speed). Using these, they were able to show (see Fig. 19) that mode-I energy release rate in unidirectional composite to be a decreasing function of crack speed.

In a more recent study, Coker and Rosakis[53] examined crack growth behaviours in unidirectional graphite/epoxy composites using reflection CGS and high-speed photography. Shear dominated fracture at high velocities was the primary focus of their work. The dynamic material characteristics for the coordinate system shown in Fig. 20 are tabulated in the accompanying table. They used an off-axis impact loading configuration (impact velocity 21 m/sec) to generate dominant shear loading at the initial notch tip. A few interferograms from their experiment are shown in Fig. 21. (In this figure, time $t = 0$ corresponds to crack initiation.) The nature of the crack tip fields suggests that the crack tip is primarily in mode-II condition prior to initiation with dominant side lobes tilted ahead of the

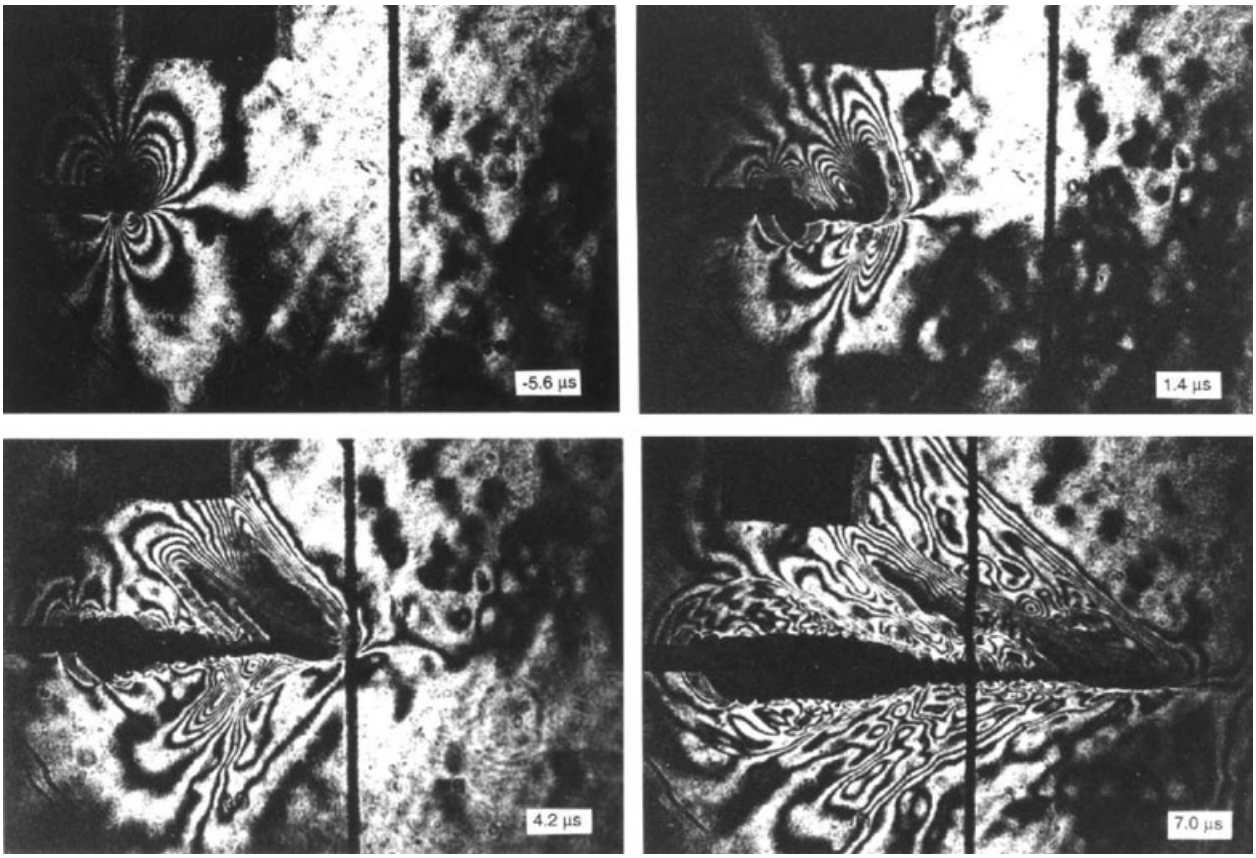

Fig. 21 A sequence of reflection CGS interferograms for shear dominated crack tip loading in a unidirectional fibre-reinforced composite. The crack growth is along the fibre direction. The time $t = 0$ corresponds to crack initiation. The crack is propagating intersonically in the last two frames. (Ref. [53], Courtesy A. J. Rosakis.)

crack tip. Soon after crack initiation, however, the fringe lobes on both the sides of the crack tilt backwards, indicating high crack speeds and acceleration. During this early period soon after crack initiation, the crack speed was estimated at ~2100 m/sec, well above the shear wave speed for the material of 1560 m/sec (see Fig. 21), and an acceleration of $\sim 10^9$ m/sec^2. As the crack continued to propagate, the shape of the fringe lobes changed even more drastically to a triangular wedge shaped region with a line of highly concentrated fringes emanating from the crack tip at a distinct angle. They associated this line to a region of high stress gradients that eventually became a stress discontinuity resulting in a shear shock wave. Based on their mode-I and mode-II crack growth observations, Rosakis and co-workers[51,53] concluded that mode-I or opening mode cracks could propagate only subsonically along the fibres with Rayleigh wave speed as the upper bound. However, mode-II or shear cracks could grow at intersonic speeds parallel to the fibres. They also observed crack acceleration from values close to shear wave speed to dilatational wave speed corresponding to the fibre direction.

CONTACT STRESS AND BEARING LOAD EVALUATIONS

A few investigators have employed CGS to study stresses and deformations near contacting bodies where stress concentration and eventual crack growth or damage often occurs. In their work on dynamic fracture mechanics of dissimilar material joints, Tippur and Xu[34] used transmission CGS and high-speed photography to estimate the impact load history on the specimen. The interference fringes near the impact point were used in conjunction with classical Flamant's solution for a line load acting on an elastic half-space. They recorded a rapid load increase of ~1750 N over a period of 80 μsec (or, a loading rate of $\sim 22 \times 10^6$ N/sec). Later on, Xu *et al.*,[54] used finite element analysis to compare their optical measurements and found good agreement. The representative interference patterns at the impact point (impact velocity ~5 m/sec) and the measured load history are shown in Fig. 22. Deformations due to dynamic impact of a rectangular rigid punch on an elastic half-space were measured by Rubio-Gonzalez and Mason[55] using CGS and high-speed photography. Their primary interest of examining punch-tip

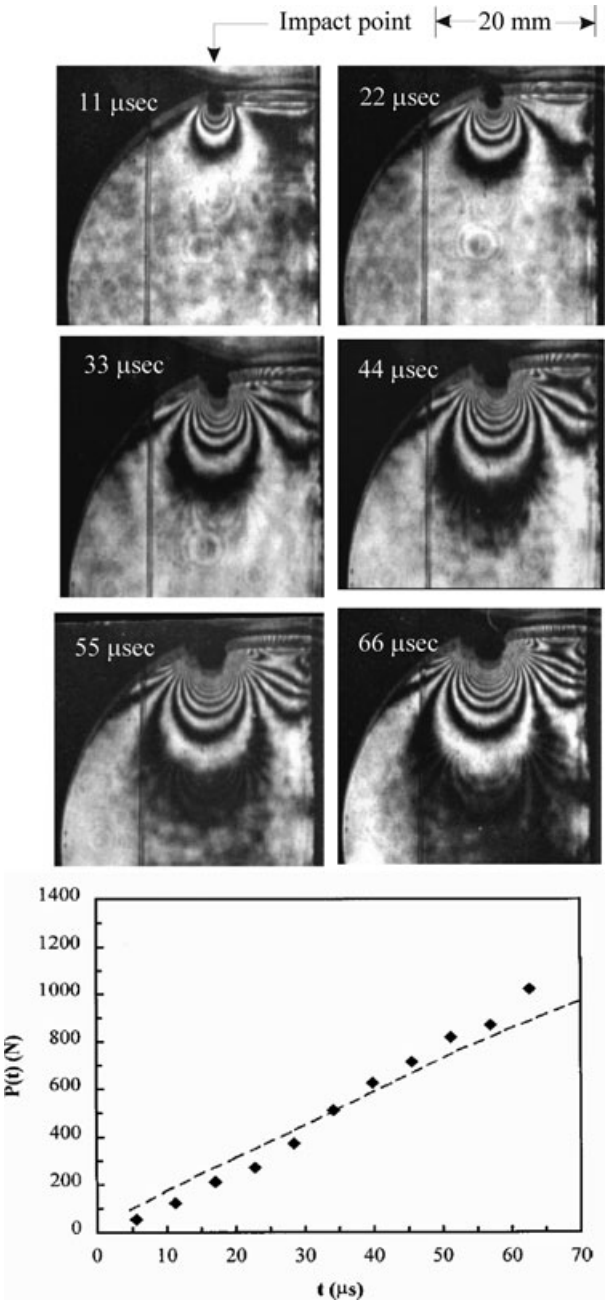

Fig. 22 Transmission CGS fringes near the vicinity of a line load acting on the edge of a PMMA sheet. The estimated contact load history $P(t)$ obtained analyzing fringes with the aid of Flamant's solution (solid symbol). The dotted line in the graph was obtained using finite element analysis.[54]

deformations was pinned on the fact that materials experience limited plasticity prior to failure requiring the knowledge of elastic stress concentration at punch corners under impact conditions. Interestingly, using an analogy between a mode-I crack tip stress field and a rectangular punch tip stress field, they deduced an equivalent stress intensity factor for the punch tip to assess failure. An optical interferogram in a PMMA sample subjected to static load using a square punch is shown in Fig. 23. Qualitative similarity between these fringes and the ones near a mode-I crack (on the left-hand and right-hand sides of the crack in Fig. 7) can be readily seen. They were able to demonstrate good agreement between measurements and theoretical predictions of punch tip stress intensity factors in both isotropic and orthotropic solids.

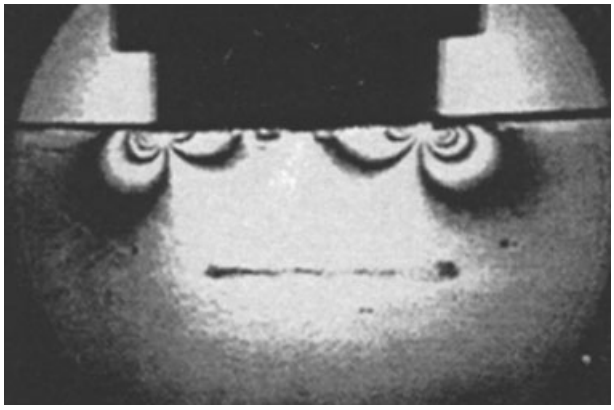

Fig. 23 Transmission CGS fringes in the vicinity of a square punch tip loading a PMMA sheet. Note the qualitative similarity between mode-I fringes near a crack tip and the punch tip.[55]

HYBRID OPTICAL TECHNIQUES INVOLVING CGS

A few investigators have successfully coupled CGS with other optical methods, such as photoelasticity, optical caustics and moiré interferometry to recover additional field quantities and/or complement CGS measurements with others. Prabhu and Lambros[56] successfully combined optical caustics and transmission CGS. They claimed that redundancy of optical data to be more useful in situations where repetition of experiments is not feasible and/or expensive. Yao *et al*.,[57] measured two sets of interferograms from the same crack tip deformation field at two different sensitivities (by using two different grating separation distances) by splitting the object wave front and processing them through two CGS interferometers simultaneously. By doing this they doubled the number of crack tip fringes for a more accurate stress intensity factor measurement.

In an interesting recent publication, Mello *et al*.,[58] have extended CGS to measure in-plane and out-of-plane displacement gradients by combining it with moiré interferometry. They replicated a high density, reflective, fine pitch cross-grating pattern on the specimen surface and illuminated it using a pair of obliquely incident collimated

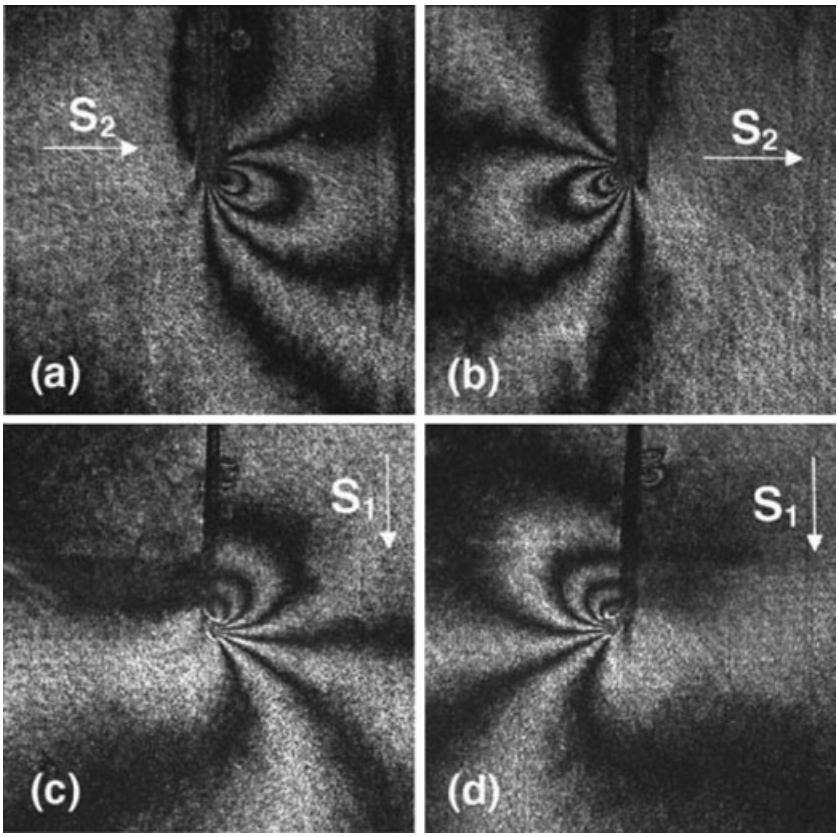

Fig. 24 CGS interferograms obtained by lateral shearing of the in-plane and out-of-plane diffracted wave fronts (generated by a specular cross-grating printed on the specimen) on along the x_1- and x_2-directions.[58]

laser beams. The resulting first-order diffractions propagating along the optical axis were prevented from interfering and instead sent through a CGS set up where each beam was sheared by a pair of Ronchi gratings. The first-order diffractions were Fourier filtered and the resulting interferograms were recorded (see Fig. 24). Subsequently phase shifting methods were implemented to generate a phase map of each differentiated wave front. By adding and substrating the two complementary phase maps through post-processing they were able to extract both in-plane and out-of-plane displacement gradients. They have implemented this novel idea to measure crack tip deformations under mode-I, mode-II and mixed-mode conditions successfully.

Another novel hybrid technique involving CGS has also been recently reported by Kramer *et al*.[59] In this work, transmission CGS was coupled with transmission photoelasticity to study a birefringent plate with a V-notch as a stress concentrator. A circularly polarized light beam was used to illuminate the specimen, which after transmission through the specimen was split into two beams using a non-polarizing beam splitter. One of the two legs of the object wave front was used for CGS and the other for photoelasticity. They employed a six-step phase shifting method to determine isoclinic (principal direction) and isochromatic (principal stress difference) parameters associated with the photoelastic measurements. To remove jumps in the phase measurements a phase unwrapping algorithm was employed. A four-step phase shifting method along with unwrapping and integration of the resulting phase provided the sum of the principal stresses. A combination all these were able to provide separated principal stresses and principal directions in the vicinity of the V-notch.

SUMMARY

In a relatively short span of 20 years, the full-field optical method of CGS has made a number of significant contributions to the field of fracture mechanics. The simplicity of implementation of the interferometer and the resulting fringe analysis are attractive features of the method. The relative insensitivity to rigid motions and vibrations has also added to its overall appeal making CGS a particularly useful method to the field of fracture mechanics in general and dynamic fracture mechanics in particular where only a handful of full-field methods have been found to be feasible.

To date CGS has contributed to the understanding of crack tip K-dominance in finite size fracture geometries and has revealed the importance of higher order terms of asymptotic mechanical fields in the analysis of

measurements near dynamically growing cracks. The method has assisted fracture mechanics investigators to make a number of the original observations pertaining to dynamic crack growth along dissimilar material interfaces such as intersonic crack growth and the conditions for such a highly transient event to occur. Many previously unknown features regarding dynamic fracture mechanics of FGM including crack path selection due to compositional gradations has been demonstrated using CGS. The method has also helped visualize of crack attraction and deflection mechanisms and quantify the associated fracture parameters when a dynamically growing crack interacts with an inclusion embedded in a matrix. Though only a few studies on dynamic fracture mechanics of fibre reinforced composites have been reported to date, the potential of CGS to this field is well demonstrated including the one regarding the possibility of supersonic crack growth in unidirectional composites under shear dominant loading. The potential of the method to study dynamic impact and load bearing problems appears to be enormous and needs attention in the coming years. The recent developments of coupling legacy CGS interferometer with other optical methods/tools show a great deal of promise and excitement. These could lead to the enhancement of CGS in terms of its versatility.

Acknowledgements

The author acknowledges the support of the National Science Foundation (Grant # CMMI-0653816) and the U.S. Army Research Office (Grant # ARMY-W911NF-08-1-0285). Assistance of Prof. A. J. Rosakis, Prof. J. Lambros and Dr. C. Liu who supplied some of the interferograms used in this review are gratefully acknowledged.

REFERENCES

1 Tippur, H. V., Krishnaswamy, S. and Rosakis, A. J. (1991) A coherent gradient sensor for crack tip measurements: analysis and experimental results. *Int. J. Fract.* **48,** 193–204 (Caltech Report SM 89-1, 1989).
2 Tippur, H. V., Krishnaswamy, S. and Rosakis, A. J. (1991) Optical mapping of crack tip deformations using the methods of transmission and reflection coherent gradient sensing: a study of crack tip K-dominance. *Int. J. Fract.* **52,** 91–117 (Caltech Report SM 89-11, 1989).
3 Tippur, H. V. (1992) Coherent gradient sensing: a Fourier optic analysis and applications to fracture. *Appl. Opt.* **31,** 4428–4438.
4 Tippur, H. V. (2004) Simultaneous and real-time measurement of slope and curvature fringes in thin structures using shearing interferometry. *Opt. Eng.* **43,** 3014–3020.
5 Rosakis, A. J., Krishnaswamy, S. and Tippur, H. V. (1990) On the application of the optical method of caustics to elasto-dynamic crack problems: limitations of the classical interpretation. *Opt. Lasers Eng.* **13,** 183–210 (Caltech Report SM 90-2, 1990).
6 Krishnaswamy, S., Tippur, H. V. and Rosakis, A. J. (1992) Measurement of transient crack tip deformation fields using the method of coherent gradient sensing. *J. Mech. Phys. Solids* **40,** 339–372 (Caltech Report SM 90-1, 1990).
7 Freund, L. B. and Rosakis, A. J. (1992) The structure of the near-tip field during transient elastodynamic crack growth. *J. Mech. Phys. Solids* **40,** 699–719.
8 Bruck, H. A. and Rosakis, A. J. (1993) On the sensititivity of coherent gradient sensing. Part-II. An experimental investigation of accuracy in fracture mechanics applications. *Opt. Lasers Eng.* **18,** 25–51.
9 Ramaswamy, S., Tippur, H. V. and Xu, L. (1993) Mixed-mode crack-tip deformations studied using a modified flexural specimen and coherent gradient sensing. *Exp. Mech.* **33,** 218–227.
10 Tippur, H. V. and Ramaswamy, S. (1993) Measurement of mixed-mode fracture parameters near cracks in homogeneous and bimaterial beams. *Int. J. Fract.* **61,** 247–265.
11 Mason, J. J., Lambros, J. and Rosakis, A. J. (1992) The use of a coherent gradient sensor in dynamic mixed-mode fracture mechanics experiments. *J. Mech. Phys. Solids* **40,** 641–661.
12 Lee, Y. J. and Freund, L. B. (1990) Fracture initiation due to asymmetric impact loading of an edge cracked plate. *J. Appl. Mech., Trans. ASME* **57,** 104–111.
13 Mason, J. J., Rosakis, A. J. and Ravichandran, G. (1994) Full-field measurements of the dynamic deformation field around a growing adiabatic shear-band at the tip of a dynamically loading crack or notch. *Mech. Mater.* **17,** 135–145.
14 Guduru, P. R., Rosakis, A. J. and Ravichandran, G. (2001) Dynamic shear bands: an investigation using high speed optical and infrared diagnostics. *Mech. Mater.* **33,** 371–402.
15 Kalthoff, J. K. and Winkler, S. (1988) Failure mode transition at high rates of loading. In: *Proceedings of the International Conference on Impact Loading and Dynamic Behavior of Materials* (Edited by C. Y. Chiem, H. D. Kunze and L. W. Meyer), Deutsche Gesellschaft fur Metallkunde, pp. 43–56.
16 Anderson, D. D. and Rosakis, A. J. (2005) Comparison of three real time techniques for the measurement of dynamic fracture initiation toughness in metals. *Eng. Fract. Mech.* **72,** 535–555.
17 Anderson, D. D. and Rosakis, A. J. (2006) Dynamic fracture properties of titanium alloys. *Exp. Mech.* **46,** 399–406.
18 Yao, X. F., Yeh, H. Y. and Xu, W. (2006) Fracture investigation at V-notch tip using coherent gradient sensing (CGS). *Int. J. Solids Struct.* **43,** 189–1200.
19 Williams, M. L. (1959) The stresses around a fault or crack in dissimilar media. *Bull. Seism. Soc. Am.* **49,** 199–203.
20 Rice, J. R. and Sih, G. C. (1965) Plane problems of cracks in dissimilar media. *J. Appl. Mech., Trans. ASME* **32,** 418–423.
21 Erodogan, F. (1965) Stress distribution in bonded dissimilar materials with cracks. *J. Appl. Mech., Trans. ASME* **32,** 403–410.
22 England, A. H. (1965) A crack between dissimilar media. *J. Appl. Mech., Trans. ASME* **32,** 400–402.
23 Liechti, K. M. and Knauss, W. G. (1982) Crack propagation at material interfaces. Part 1. Experimental technique to determine crack profiles. *Exp. Mech.* **22,** 262–269.
24 Tippur, H. V. and Rosakis, A. J. (1991) Quasi-static and dynamic crack growth along bimaterial interfaces: a note on crack tip field measurements using coherent gradient sensing. *Exp. Mech.* **31,** 243–251.

25 Goldshtein, R. V. (1967) On surfaces in joined elastic materials and their relation to crack propagation along the junction. *Appl. Math. Mech.* **31,** 496–502.
26 Brock, L. M. and Achenbach, J. D. (1973) Extension of an interface flaw under the influence of transient waves. *Int. J. Solids Struct.* **9,** 53–67.
27 Willis, J. R. (1973) Self similar problems in elastodynamics. *Phil. Trans. Roy. Soc. London* **274,** 435–491.
28 Atkinson, C. (1977) Dynamic problems in dissimilar media. In: *Mechanics of Fracture 4: Elasto-Dynamic Crack Problems* (Edited by G. C. Sih), Noorhoff, Leyden, pp. 213–248.
29 Yang, W., Suo, Z. and Shih, C. F. (1991) Mechanics of elastodynamic debonding. *Proc. Roy. Soc. London* **A433,** 679–697.
30 Liu, C., Lambros, J. and Rosakis, A. J. (1995) Shear dominated transonic interfacial crack growth in a bimaterial. Part II. Asymptotic fields and favorable velocity regimes. *J. Mech. Phys. Solids* **43,** 189–206.
31 Liu, C., Lambros, J. and Rosakis, A. J. (1993) Highly transient elastodynamic crack growth in a bimaterial interface: higher order asymptotic analysis and experiments. *J. Mech. Phys. Solids* **41,** 1887–1954.
32 Lambros, J. and Rosakis, A. J. (1995) Dynamic decohesion of bimaterials: experimental observations and failure criteria. *Int. J. Solids Struct.* **32,** 2677–2702.
33 Xu, L. M. and Tippur, H. V. (1995) Fracture parameters for interfacial cracks– an experimental-finite element study of crack-tip fields and crack initiation toughness. *Int. J. Fract.* **71,** 345–363.
34 Tippur, H. V. and Xu, L. M. (1997) Interfacial crack initiation under quasi-static and dynamic loading conditions: an experimental study. *J. Fatigue Fract. Eng. Mater. Struct.* **20,** 49–60.
35 Kimberley, J. and Lambros, J. (2004) Dynamic crack kinking from a PMMA/homalite interface. *Exp. Mech.* **44,** 158–166.
36 Kitey, R. and Tippur, H. V. (2005) Role of particle size and filler-matrix adhesion on dynamic fracture of glass-filled epoxy. Part I. Macromeasurements. *Acta Mater.* **53,** 1153–1165.
37 Kitey, R. and Tippur, H. V. (2008) Dynamic crack growth past a stiff inclusion: optical investigation of inclusion eccentricity and inclusion-matrix adhesion strength. *Exp. Mech.* **48,** 37–54.
38 Koizumi, M. (1995) Overview of FGM research in Japan. *MRS Bull.* **20,** 19–21.
39 Butcher R. J., Rousseau, C. E. and Tippur, H. V. (1998) A functionally graded particulate composite: preparation, measurements and failure analysis. *Acta Mater.* **47,** 259–268.
40 Rousseau, C.E. and Tippur, H. V. (2000) Compositionally graded materials with cracks normal to the elastic gradient. *Acta Mater.* **48,** 4021–4033.
41 Rousseau, C.-E. and Tippur, H. V. (2001) Dynamic fracture of functionally graded materials with cracks along the elastic gradient: experiments and analysis. *Mech. Mater.* **33,** 403–421.
42 Rousseau, C.-E. and Tippur, H. V. (2002) Evaluation of crack tip fields and stress intensity factors in functionally graded elastic materials: cracks parallel to elastic gradient. *Int. J. Fract.* **114,** 87–111.
43 Marur, P. R. and Tippur, H. V. (2003) Dynamic response of bimaterial and graded interface cracks under impact loading. *Int. J. Fract.* **103,** 95–109.
44 El-Hadek, M. A. and Tippur, H. V. (2003) Dynamic fracture behavior of syntactic epoxy foams: optical measurements using coherent gradient sensing. *Opt. Lasers Eng.* **40,** 353–369.
45 Kirugulige, M. S., Kitey, R. A. and Tippur, H. V. (2005) Dynamic fracture behavior of model sandwich structures with functionally graded core: a feasibility study. *Compos. Sci. Technol.* **65,** 1052–1068.
46 Rousseau, C.-E. (2006) Critical examination of the use of coherent gradient sensing in measuring fracture parameters in functionally graded materials. *J. Compos. Mater.* **40,** 1763–1782.
47 Parameswaran, V. and Shukla, A. (1999) Crack-tip stress fields for dynamic fracture in functionally gradient materials. *Mech. Mater.* **31,** 579–596.
48 Kirugulige, M. S. and Tippur, H. V. (2006) Mixed-mode dynamic crack growth in functionally graded glass-filled epoxy. *Exp. Mech.* **46,** 269–281.
49 Kirugulige, M. S. and Tippur, H. V. (2008) Mixed-mode dynamic crack growth in a functionally graded particulate composite: experimental measurements and numerical simulations. *ASME J. Appl. Mech.* **75,** 1–14.
50 Liu C., Rosakis A. J., Ellis R. W. and Stout M. S. (1998) A study of the fracture behavior of unidirectional fiber-reinforced composites using coherent gradient sensing (CGS) interferometry. *Int. J. Fract.* **90,** 355–382.
51 Lambros, J. and Rosakis, A. J. (1997) Dynamic crack initiation and growth in thick unidirectional graphite/epoxy plates. *Compos. Sci. Technol.* **57**, 55–65.
52 Liu, C., Rosakis, A. J. and Stout, M. S. (2001) Dynamic fracture toughness of a unidirectional graphite/epoxy composite. In: *Proceedings of the Symposium on 'Dynamic Effects in Composite Structures', Proceedings of ASME-IMECE, AMD.* **247**, pp 1–12. New York, NY.
53 Coker, D. and Rosakis, A. J. (2001) Experimental observation of intersonic crack growth in asymmetrically loaded unidirectional composite plates. *Philos. Mag., A* **81,** 571–595.
54 Xu, L., Tippur, H. V. and Rousseau, C.-E. (1999) Measurement of contact stresses using real-time shearing interferometry. *Opt. Eng.* **38,** 1932–1937.
55 Rubio-Gonzalez, C. and Mason, J. J. (2001) Experimental investigation of dynamic punch tests on isotropic materials and fiber reinforced composites. *Exp. Mech.* **41,** 129–139.
56 Prabhu, S. and Lambros, J. (2000) A combination of optical method of lateral shearing interferometry and caustics. *Exp. Mech.* **40,** 376–383.
57 Yao, X. F., Xu, W. and Yeh, H. Y. (2006) Improvement of measurement error for modified coherent gradient sensing. *Meas. Sci. Technol.* **17,** 1491–1495.
58 Mello, M., Hong, S. and Rosakis, A.J. (2009) Extension of the coherent gradient sensor to the combined measurement of in-plane and out-of-plane displacement field gradients. *Exp. Mech.* **49,** 277–289.
59 Kramer, S. L. B., Mello, M. Ravichandran, G. and Bhattacharya, K. (2009) Phase shifting full-field interferometric methods for determination of in-plane tensorial stresses. *Exp. Mech.* **49,** 303–315.